2009

Delta Relaxation Enhanced Magnetic Resonance

Jamu K. Alford

Delta Relaxation Enhanced Magnetic Resonance

(Spine title: Delta Relaxation Enhanced Magnetic Resonance)

(Thesis format: Integrated-Article)

by

Jamu K. Alford

Graduate Program in Physics

A thesis submitted in partial fulfillment

of the requirements for the degree of

Doctor of Philosophy

The School of Graduate and Postdoctoral Studies

The University of Western Ontario

London, Ontario, Canada

Abstract

Generally speaking, targeted molecular imaging has always been difficult to perform with magnetic resonance. The difficulty does not arise with the magnetic resonance imaging (MRI) technique or equipment itself, but rather with the targeted contrast agents, which the method requires. Also referred to as activatable contrast agents, or MRI probes, targeted contrast agents are pharmaceuticals that will selectively bind to a particular biological (target) molecule. They are used to highlight a certain tissue or the difference between healthy and diseased tissue. Unfortunately, nearly all MRI probes are non-specific, causing localized increases in MR image intensity in both the unbound and target-bound states. Therefore, brightening in a conventional MRI image, following probe injection, does not positively indicate the presence of the target molecule.

Herein, a novel method known as delta relaxation enhanced magnetic resonance (dreMR, pronounced "dreamer") is presented that utilizes variable magnetic field technology to produce image contrast related to the dependence of the sample's longitudinal relaxation rates upon the strength of the main magnetic field of the MRI scanner. Since only bound contrast agent shows significant magnetic field dependence, it is an indicator of the bound probe, which is in turn a marker for the target molecule.

This work details the development of the dreMR method, focusing on the specialized hardware necessary to provide a clinical, static-field MRI the ability to modulate its main magnetic field throughout an MRI sequence. All modifications were performed in such a manner that the host MRI system was not degraded or

Acknowledgments

Many individuals contributed to the success of this project. My Supervisor, Dr. Blaine Chronik, provided the guidance, the freedom and the opportunity necessary to make this work so successful.

I am extremely grateful for the daily assistance of our group's research associates, Drs. Timothy Scholl and William Handler. I could not have done this without them.

Our collaborator, Dr. Brian Rutt, provided many of the initial insights into what eventually became the dreMR method. His idea of using an inversion recovery sequence to suppress tissue signal was instrumental in the eventual development of the double inversion recovery dreMR pulse sequence.

Finally, I would like to thank Mr. Brian Dalrymple and Mr. Frank Van Sas for their tireless patience and invaluable advice during the construction of both dreMR systems.

Dedication

For my mother Sandy, wife Jacqueline and daughter Zoe. The 2 and ½ women who have taken care of me for so long.

Co-authorship

This thesis contains material from previously published journal articles co-authored by Jamu Alford, William Handler, Timothy Scholl, Brian Rutt, and Blaine Chronik. Versions of the original journal articles, which appear in Chapters 2 and 3, were written by Jamu Alford. Copyright releases for these articles are shown in Appendix A. All theoretical and experimental work presented here was performed by Jamu Alford with the following exceptions: The radio frequency coil used in Chapters 2, 3 was built by Mr. Andrew Alejski. The radio frequency coil discussed in Chapter 4 and the computer aided drawings of the dreMR system shown in Chapter 4 were the sole work of Timothy Scholl. Assistance in building the dreMR systems was provided by Brian Dalrymple, Frank Van Sas, Timothy Scholl, William Handler and Doug Hie.

Table of Contents

Table of Abbreviations

AWG	American Wire Gauge
CSF	Cerebral Spinal Fluid
dreMR	Delta Relaxation Enhanced Magnetic Resonance
DIR	Double Inversion Recovery
DTPA	Diethylenetriamine Penta-acetic Acid
Gd	Gadolinium
GRE	Gradient Recalled Echo
IGBT	Insolated Gate Bipolar Transistor
MR	Magnetic Resonance
MRI	Magnetic Resonance Imaging
NMR	Nuclear Magnetic Resonance
PBS	Phosphate Buffer Saline
RF	Radio Frequency
RSA	Rabbit Serum Albumin
SNR	Signal to Noise Ratio
SPGR	Spoiled Gradient Echo
TE	Echo Time
TR	Repetition Time
WM	White Matter
GM	Grey Matter

Chapter 1 – Introduction to MRI

(1.1) Introduction

This work details the development of a novel, magnetic resonance (MR) based, molecular imaging method called **d**elta **r**elaxation **e**nhanced **M**agnetic **R**esonance (dreMR, pronounced "dreamer"). DreMR is both a device and a method. As a device, dreMR combines the unique features of field-cycled magnetic resonance imaging (MRI) with the availability and image quality of superconducting MRI systems. As a method, dreMR prepares image contrast related to the concentration of targeted contrast agents (probes), which have become bound to their target molecules. DreMR determines probe binding by exploiting the dependence of the longitudinal magnetization rates (R_1) upon magnetic field strength. Appreciable magnetic field dependence in R_1 is only present following the binding of an exogenous contrast agent to its target molecule. Specialized dreMR hardware is necessary to make use of this feature, since the manipulation of any magnetic field dependent parameter requires the ability to dynamically change the magnetic field. This introductory chapter provides the necessary background for understanding both MRI and this method. We introduce magnetic resonance imaging, describe the specialized disciplines of field-cycled relaxometry and field-cycled MRI, present the necessary background on the principles of magnetic relaxation, and discuss the role of MRI contrast agents in increasing relaxation. Chapter One ends with a brief overview of the thesis.

(1.2) Introduction to MRI Concepts

MRI is a powerful and highly complex imaging modality with both research and clinical applications. For brevity, this chapter will introduce certain MRI concepts often omitted from introductory MRI texts, while excluding other details that are sufficiently described in literature. The reader is recommended to *"Magnetic Resonance Imaging" by Haacke et al., John-Wiley and Sons, 1999* and *"Spin Dynamics, 2nd Edition" by M.H. Levitt, John-Wiley and Sons, 2008.*

Magnetic resonance imaging relies on the interactions of systems of nuclear spin with applied magnetic fields. While spin is most accurately described within the framework of quantum mechanics, in many cases the classical approximation is sufficient. Though not entirely complete, the classical explanation is intuitive and will serve our purposes here.

(1.2.1) Bulk Magnetization

When protons are subjected to a magnetic field the magnetization due to their magnetic dipole moments will obtain a bulk alignment parallel to the magnetic field. Due to the high thermal energy present in the living human body, the magnetic dipole moment of any particular proton could be at any angle to the applied field. It is only for large quantities of protons that a bulk magnetization appears. Within the bulk magnetization each individual proton will precess, or resonate, at a highly specific

frequency call the Larmor frequency. The Larmor frequency, f, varies linearly with the magnetic field strength and is given by the simple equation,

$$f = {}^{\gamma}/_{2\pi} \cdot B. \qquad [1.1]$$

Here, *B* is the applied field in Tesla and $\gamma/2\pi$ is called the gyromagnetic ratio in the units of Hz/Tesla. For the proton, the gyromagnetic ratio is 42.58 MHz/Tesla. For conventional MRI systems the Larmor frequency of protons is within the radiofrequency range and scales with the strength of the main magnetic field. The main magnetic field vector in an MRI experiment is widely referred to as $\mathbf{B_0}$, which by convention is in the direction chosen for the *z*-axis. Figure 1.1 below illustrates the collective behavior of protons in an applied magnetic field.

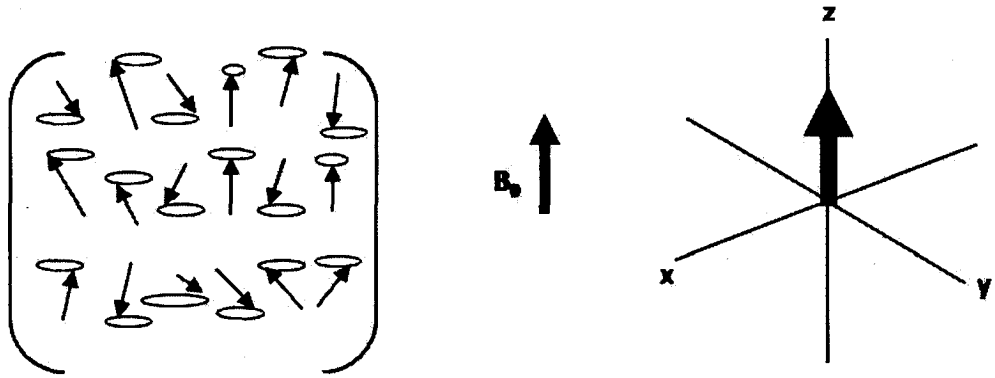

Figure 1.1 Left: Magnetic moments of a population of hydrogen atoms in a static magnetic field at room temperature. Each magnetic moment precesses around the *z*-axis like a top in a gravitational field. Right: The net magnetization is aligned with the magnetic field vector $\mathbf{B_0}$.

The of the bulk magnetization, $\mathbf{M_0}$, depends directly upon the number of protons per unit volume, ρ, the gyromagnetic ratio, γ, magnetic field, $\mathbf{B_0}$ and inversely with temperature, T. In Eq. 1.2, $\hbar$ bar is Planck's constant divided by 2π and k is Boltzmann's constant.

$$\mathbf{M_0} = \frac{\rho\gamma^2\hbar^2}{4kT}\mathbf{B_0} \qquad [1.2]$$

(1.2.2) Detection of Magnetization

Even for a macroscopic sample containing an Avogadro's number of spins, a further step must be taken to produce a detectable signal. In the classical mechanic description, the bulk magnetization vector, $\mathbf{M_0}$, must be tipped perpendicular to the applied magnetic field. Once it is no longer parallel to $\mathbf{B_0}$, $\mathbf{M_0}$ will precess about $\mathbf{B_0}$. The precessing of the bulk magnetization produces a time varying magnetic flux that, by Faraday's law, generates a voltage in a nearby radio frequency (RF) 'receiver' coil. The resulting signal in the RF coil will oscillate at the Larmor frequency and possess an amplitude dependent upon the magnitude of the bulk magnetization. The 'tipping' of the bulk magnetization is achieved by application of a time-varying magnetic field fluctuating close to the Larmor frequency. This RF 'excitation' pulse is generally produced by an RF 'transmit' coil, which may be the same coil as the receive coil. The angle between the z-axis and bulk magnetic moment vector is called the flip angle and is a function of the duration,

power and envelope of the RF pulse. Figure 1.2 shows the effect of weak and strong RF pulses on a bulk magnetization.

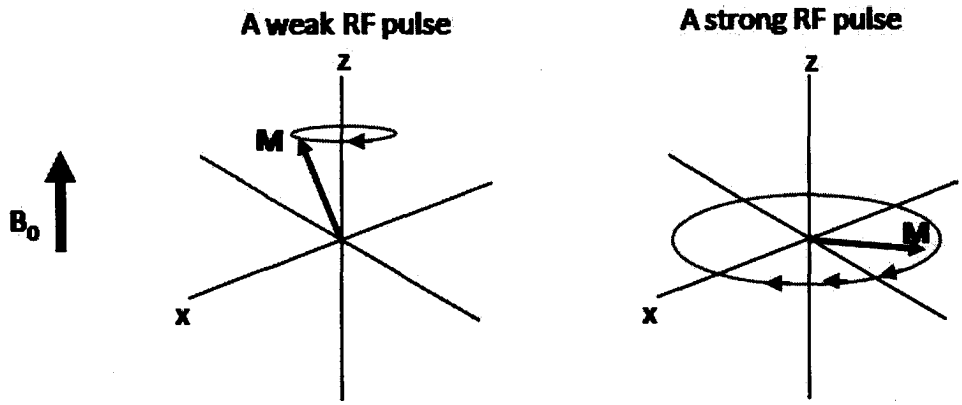

Figure 1.2. A weak RF pulse causes the bulk magnetic moment to precess around the *z*-axis with a small flip angle while a strong RF pulse causes a 90° flip angle.

Following the RF pulse, the magnetization vector precesses in the transverse plane creating a voltage signal in the RF coil at the Larmor frequency of the sample. Within a few seconds following the end of the RF pulse the bulk magnetic moment has returned to its equilibrium alignment with the z-axis and the induced voltage disappears from the receiver coil.

(1.2.3) Relaxation Times

The relaxation, or regrowth, of the bulk longitudinal magnetization following a rotation into the transverse plane is called longitudinal or 'spin-lattice' relaxation and is a result of interactions between the protons and their environment. The rate of regrowth is

characterized by the time constant T_1. Following the application of a 90° pulse the subsequent regrowth of the *z*-component of magnetization, *Mz*, is given by

$$M_z = M_0\left(1 - e^{-t/T_1}\right). \qquad [1.3]$$

While the longitudinal relaxation grows towards M_0, the transverse magnetization ($M_\perp$) decreases exponentially due to the dephasing, or decorrelation, of spins throughout the ensemble. This process is usually referred to as spin-spin decay or transverse relaxation. The dispersion of phase is a result of variations in the processional frequency due to local magnetic field variations. If the transverse magnetization of a sample was measured at a time, T_E, (echo-time) following a longitudinal regrowth of duration T_R (repeat-time) then the transverse magnetization would have the form

$$M_\perp = M_0\left(1 - e^{-T_R/T_1}\right)e^{-T_E/T_2}. \qquad [1.4]$$

Equation 1.4 illustrates an important feature in MRI, namely that image contrast, which arises from $M_\perp$, is not simply an indication of proton densities, but can be easily adjusted to reflect differences in the relaxation times, T_1 and T_2, by judicious choice of T_R and T_E. Proton density, T_1 and T_2 are the principle forms of MRI contrast in diagnostic imaging.

(1.2.4) Contrast Agents

Contrast agents are pharmaceuticals that are commonly used in MRI to enhance specific tissues or the difference between healthy and diseased tissue by changing the relaxation time constant of one tissue over the other. The most common form of clinically applicable contrast agents are referred to as T_1-shortening or 'brightening' agents. These agents are typically gadolinium chelates that will shorten the T_1 times of nearby protons and cause localized brightening in the MRI image. Generally, these contrast agents are used as "blood pool agents" to shorten the T_1 of blood in order to enhance arterial and vascular structures. The gadolinium chelate has two parts, the gadolinium ion, which shortens relaxation and the chelate, which can serve multiple purposes. Primarily it reduces the toxicity of the gadolinium ion. However, in certain applications, the chelate is modified to include targeting vectors to selectively bind to certain target molecules. Targeting vectors could include antibodies, protein structures, DNA and RNA complexes, etc. In some applications, targeting is used to detect specific molecules while in others it reduces the rate at which the agent is removed by biological processes. As we will see shortly, the process of binding significantly changes the magnetic properties of the agents.

Once one begins to discuss contrast agents, it is often more convenient to use the relaxation rates R_1 and R_2 given by $1/T_1$ and $1/T_2$ respectively, to describe longitudinal and transverse relaxation. Relaxation rates, resulting from different relaxation mechanisms, are summed to produce the total relaxation rate. For example,

the relaxation rate of water in the presence of a gadolinium ion is equal to the relaxation rate of the water plus the relaxation rate of the ion, i.e. $R_1 = R_1^{water} + R_1^{ion}$.

(1.2.5) Relaxation

To understand how contrast agents work, we must examine the process by which bulk magnetization occurs. Within the time scale of a normal MRI experiment (minutes to hours), individual protons do not spontaneously relax from a high-energy state (anti-parallel to the applied field) to a low energy state (aligned with the magnetic field). This transition must be stimulated by an electromagnetic field, oscillating at the Larmor frequency of the sample.

The magnetic moments of nearby electrons and protons are the source of the oscillating magnetic field. Thermal energy in the sample produces Brownian motion of molecules in the sample. Random displacement and rotation of particles results in a spectrum of oscillating magnetic field energies. When two hydrogen protons interact to produce mutual relaxations it is called homonuclear relaxation. Conversely, relaxation mediated by a magnetic field from some other source, such as a gadolinium chelate, is heteronuclear.

The interaction of a proton with the fluctuating magnetic fields produced by neighboring particles is commonly referred to as dipole-dipole interaction. These particles may be electrons or other protons. The three parameters of dipole-dipole

interaction that are particularly important are: the strength of the magnetic moments, the separation of the dipoles and the relative motion of the dipoles.

The magnitude of each of the dipoles influences the strength of the dipole-dipole interaction. Two typical sources of heteronuclear dipole-dipole interactions are proton-electron and proton-gadolinium (Gd^{3+}). Equation 1.5 shows the relation between spin (S), magnetic moment (μ), Planck's constant (h) and gyromagnetic ratio

$$\mu = \left(\frac{\gamma}{2\pi}\right) h\sqrt{S(S+1)}. \qquad [1.5]$$

The separation distance of the dipoles also influences the dipole-dipole interaction. Since the magnetic field of a dipole decreases as the cube of the distance, the interaction between dipoles decreases inversely as the sixth power of their separation. This consideration is paramount in the design of gadolinium based contrast agents, which utilize chelate molecules to lower toxicity. Chelates are soluble chemicals, which will contain and reduce the toxicity of a metal ion. If the physical extent of the chelate increases the dipole-dipole separation by 10% then the interaction strength is reduced by a factor of 44%.

The Brownian motion of the magnetic dipoles is an important factor in R_1 and R_2 relaxation (1). The magnetic field produced by each dipole in the sample can be viewed as a small magnetic field inhomogeneity. Relatively static inhomogeneities dephase

transverse magnetization ($M_\perp$) in exactly the same manner as any other static field inhomogeneity. The degree of dephasing between two spins depends upon the duration that the dipoles remain at the same spacing and orientation. This explains the short T_2 (fast transverse magnetization decay) in tissues with stationary protons compared to tissues with highly mobile molecules.

(1.2.6) Spectral Density and Correlation Times

The probability that a magnetic moment, associated with a particular molecule, will maintain a given orientation over a period of time, *t*, is given by the correlation function, e^{-t/τ_c}, where τ_c is called the correlation time. Smaller molecules have shorter correlation times than large molecules, suggesting that they produce a higher frequency of magnetic oscillation.

Oscillations do not occur at a single frequency, but over a spectrum of frequencies described by the spectral density distribution function. The spectral density function, $\mathbb{J}(\omega, \tau_c)$, is the Fourier transform of the rotational correlation function. This function describes the relative spectral energy at each frequency for a molecule with correlation time τ_c

$$\mathbb{J}(\omega, \tau_c) = \int_0^\infty d\tau \cdot e^{-\frac{\tau}{\tau_c}} \cdot e^{-i\omega\tau} \propto \frac{\tau_c}{1+(\omega \cdot \tau_c)^2}. \qquad [1.6]$$

In Figure 1.3 the spectral density function given by Equation 1.6 is plotted for two tumbling dipoles, one with a correlation time of 10 ns and the other with a correlation time of 10 ps. In both cases, the magnetic field fluctuations are concentrated at frequencies below the half power frequency, $f_{1/2} = 1/(2\pi \cdot \tau_c)$.

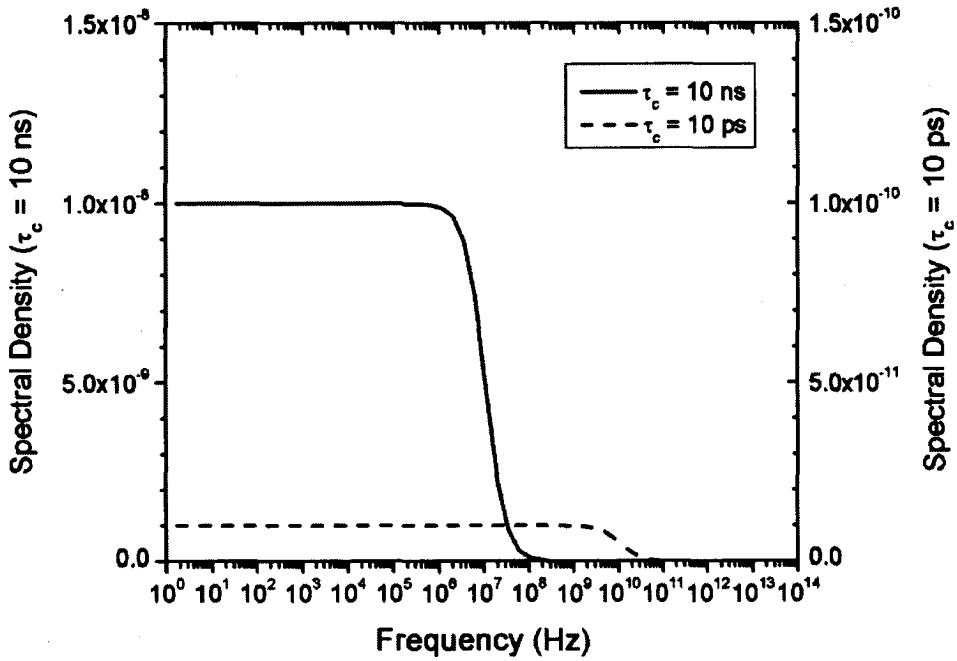

Figure 1.3. The spectral density of magnetic field fluctuations is plotted for two different molecules with rotational correlations times of 10 ns and 10 ps. Note that when the correlation time is small the spectral density is lower and spread over a wider range of frequencies.

The binding of a relatively small contrast agent to a larger, *in vivo* molecule slows it rotational rate, increasing its correlation time. Such a change in correlation time significantly changes the spectral energy produced by the agent's magnetic dipole

increasing the relaxation rates of nearby water protons. Let us treat the two spectral density curves show in Figure 1.3 as belonging to a single MRI probe that is either in the unbound state, with a 10 ps correlation time, or in the bound state with a 10 ns correlation time. In the unbound state, the spectral density curve is nearly flat in the frequency range of 1 MHz to 1000 MHz. This range is important since nearly all modern MRI experiments occur in this band. Conversely, in the bound state the spectral energy density varies strongly with frequency (magnetic field). The energy density is much higher at low frequencies, and significantly lower at high frequencies. In this bound state, the energy density is highly dependent upon the magnetic field. This suggests that it would be possible to determine the binding state of the probe by measuring the change in relaxation rate (spectral energy) with magnetic field strength. Though spectral energy is not directly measured, it is observed indirectly in an agent's ability to increase the relaxation rate of surrounding protons. The measure of this ability is called relaxivity. The longitudinal relaxation rate of a tissue which has taken up a contrast agent of concentration [*CA*] and relaxivity r_1 can be written as, $R_{1Measured} = R_{1Unenhanced} + r_1 \cdot [CA]$. Concentration is typically stated in units of milli-moles per liter.

Of a number of lanthanide-based probes surveyed (2-6) all demonstrated a change in the magnetic field dependence of relaxivity between the unbound and bound state. In Figure 1.4 the relaxivities of the clinically approved agent MS-325 (marketed under the name Vasovist by Bayer) is shown in the unbound and bound state. In the

unbound state the relaxivity of the agent is basically independent of the magnetic field strength. However, upon binding to its target molecule, human serum albumin, (67 kDa) the tumbling rate falls and the relaxivity both increases and becomes extremely field dependent. This is the basic premise of dreMR: By measuring the field dependence of the relaxivity of an agent it is possible to determine whether the agent is in the bound or unbound state. For an agent that is specific to a particular target molecule, the bound state is an unambiguous indication of the presence of the target molecule.

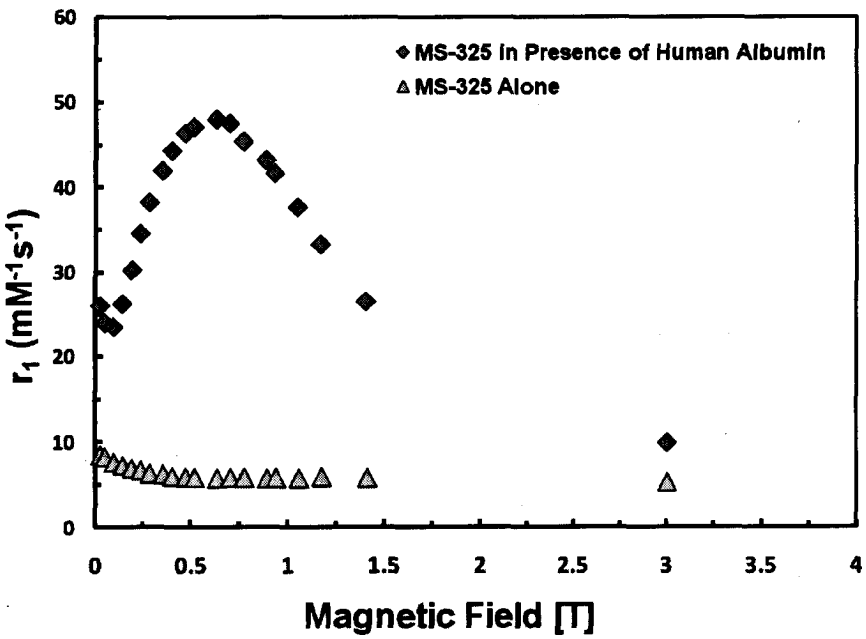

Figure 1.4. The relaxivity of a contrast agent indicates its ability to increase relaxation rates per milli-molar concentration. The agent MS-325 (marketed under the name Vasovist) possess a strong field dependence when it has bound to it target molecule human serum albumin. In the unbound state the probe shows very little field dependence. Data obtained through private correspondence with Dr. Peter Caravan at Massachusetts General Hospital.

There are certain differences between the ideal spectral energy densities shown in Figure 1.3 and the relaxivities in Figure 1.4, especially at magnetic field strengths below 0.5 T. However, above 0.5 T, the connection between relaxivity and spectral energy density is very strong. There are mathematical models for relating both the relaxivity of agents and the relaxation rates of biological tissues with spectral density. The Solomon, Bloembergen and Morgan equations are the traditional starting point for these models and are well described in a number of available texts (7-9). I do not intend to repeat these derivations or proofs, but rather state a simple approximation that is sufficient for the purpose of this work: Both relaxation rates and relaxivities depend strongly upon the spectral density function. As the magnetic field increases, there is a decreasing amount of available spectral energy and therefore relaxation rates and relaxivities generally decrease. The spectral density of large, slowly rotating molecules decreases quickly with frequency while small, quickly rotating molecules also exhibit a decrease in spectral density but less dramatically.

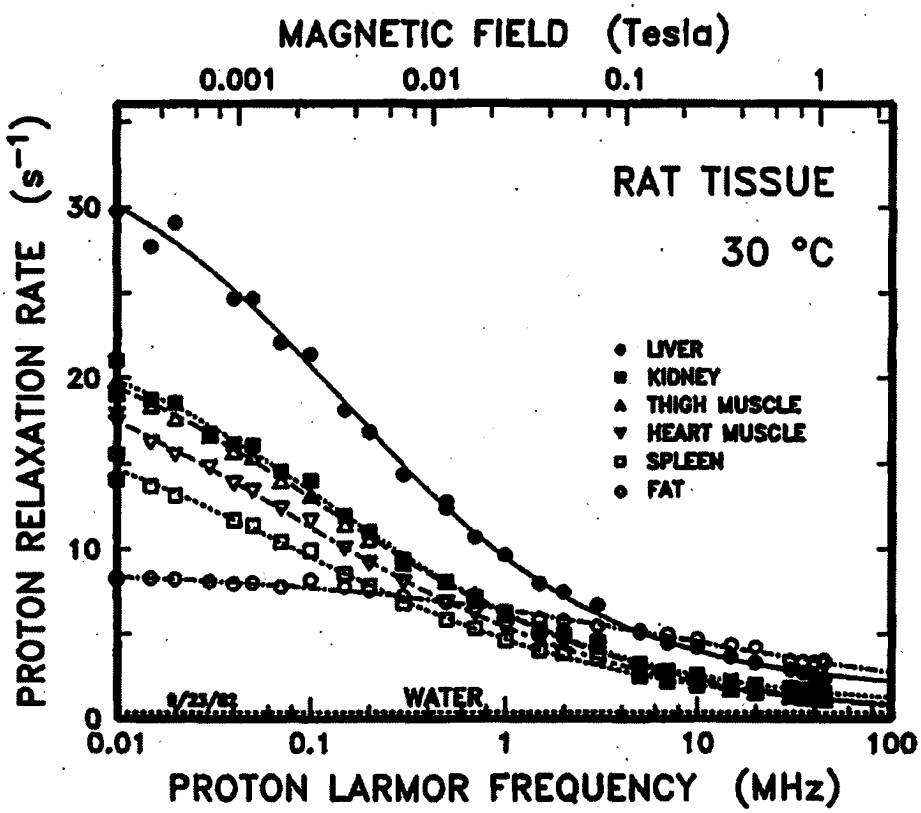

Figure 1.5. The relaxation rates of various tissues as a function of magnetic field strength. At lower field strength there is greater variation across the tissues. At higher field strengths the tissue slopes (dR1/dB) become increasingly flat. Reprinted with permission: Koenig, et al. Magnetic field dependence of 1 / T1 of protons in tissue. Investigative Radiology 1984;19(2):76-81

In Figure 1.5, the relaxation rates vs. magnetic field strength are shown for six tissues. Initially the relaxation rates of the tissues fall quickly with field, however at field strengths above 0.1 T (~4 MHz) the observed field dependence begins to lessen. At 1.5 T the magnetic field dependences of R_1 are nearly zero (flat slope). This observation will be a key argument (presented later in this thesis) for the development of dreMR. With

dreMR we want to associate any magnetic field dependence in relaxation rates with bound agent and not with biological tissues.

(1.2.7) Field-Cycled Relaxometry

The relaxation rates, R_1 and R_2, are both dependent on the strength of the applied magnetic field. Therefore, an R_1-weighted image taken at 1.5 Tesla (T) will display a slightly different tissue-tissue contrast than an 'equivalent' R_1 weighted image taken at 3.0 T. The research area of field-cycled relaxometry (11) studies the dependence of longitudinal (R_1) relaxation rates upon the strength of the applied magnetic field. Since the field dependence of biological tissues is greatest at low field strength, relaxometry devices typically work at field strengths ranging from 1 μT to 1 T. Unlike MRI, where images are produced contrasting the differences between tissue types, relaxometry measures properties of small homogenous samples. Although relaxometry is often used to study material properties, contrast agents and fluid interfaces, it also has medical applications (12,13). For example, in 2000 (14) it was demonstrated that the dependence of R_1 on magnetic field strength for the substantia nigra pars compacts could be used as a biomarker for Parkinson's disease.

A field-cycled relaxometry device measures relaxation rates by rapidly modulating the strength of the magnetic field during a series of relaxivity measuring experiments. Because both RF transmit and RF receive coils are narrowly tuned to a specific frequency (field strength), the frequency of precession of the sample must be

brought to match the RF coil frequency both for both excitation and measurement. Therefore, a field-cycled relaxometer device requires the ability to quickly change the strength of the magnetic field experienced by the sample from the RF field strength to the relaxation field strength and back again. By taking a series of measurements with different relaxation times and at different magnetic field strengths, it is possible to generate a nuclear magnetic resonance (NMR) dispersion curve, where R_1 is accurately determined for many magnetic field strengths.

(1.2.8) Field-Cycled Imaging

Taking field-cycled relaxometry one-step further is the niche research area of field-cycled imaging (also-called prepolarized MRI or pMRI) (15-17). This technique combines the imaging methods of MRI with the magnetic field shifting requirement of field-cycled relaxometry. There are several different methods to perform field-cycled imaging. In one method (18,19), a static field MRI system consisting of either a superconducting magnet or permanent magnet is modified (permanently) (20) to include an auxiliary electromagnet. During the portion of the imaging sequence when the sample magnetization magnetically interacts with the RF coil (excitation or measurement), the electromagnet is disabled and the total magnetic field is determined by the static magnet. However, during the relaxation portion of the MRI experiment, the electromagnet is used to modify the strength of the applied magnetic field. This approach has been used (15-20) to produce image contrast related to the magnetic field

dependence of tissue relaxation rates. For the second method of field-cycled MRI, two dynamically controlled, resistive magnets are used. One magnet, the polarizing magnet, is responsible for magnetizing the sample. The field from this magnet field needs to be strong, but not particularly uniform or stable. The other magnet, the readout magnet, is required during the detection of the precessing magnetization. The field from this magnet needs to be both stable and uniform, but not particularly strong. Contrast and signal to noise ratios (SNR) in field-cycled MR images depend on a combination of the polarizing field waveform, the readout field waveform, the RF and gradient waveforms, and the sample characteristics. An example pulse sequence is shown in Figure 1.6.

Though field-cycled MRI carries the allure of an additional dimension of information, which is unattainable with static field MRI systems, it is basically ignored by MRI manufactures because of difficulties in producing strong, stable and homogenous magnetic fields that can be readily controlled. As well, since unenhanced biological tissues show very little field dependence at clinical field strength, varying the magnetic field would obtain little useful information. It is only with targeted contrast agents where the ability to vary the magnetic field carries the promise of additional, important information.

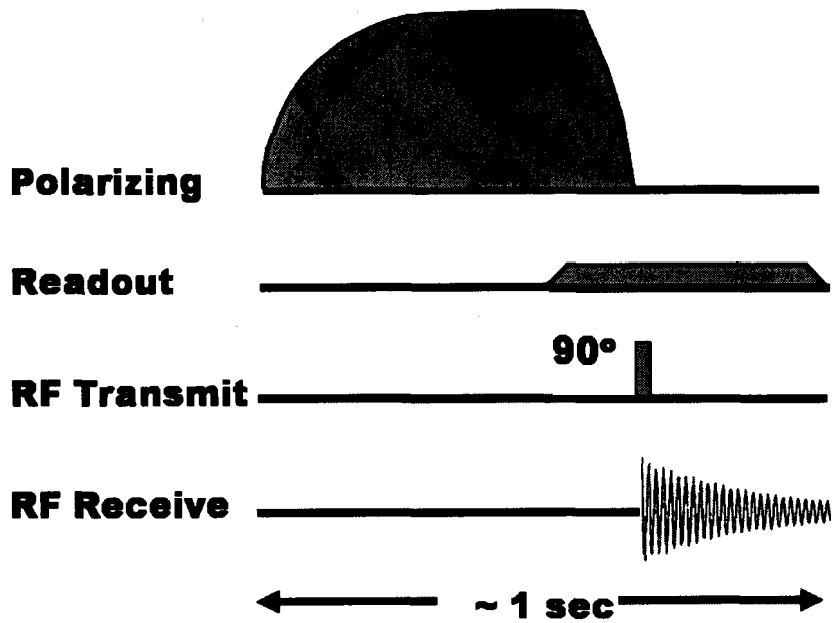

Figure 1.6. A typical pulse sequence for a field-cycled MRI machine is shown. The polarizing field is first turned on to magnetize the sample. At the end of the polarizing pulse, the readout field is turned on to produce a uniform field for signal detection. Before signal acquisition can begin the readout field must be allowed to stabilize. The gradient and some RF pulses are not shown for simplicity.

Of the two types of field-cycled MRI discussed above, the hardware development described in this thesis resembles the first type; but rather than permanently modifying an MRI system, a removable insert is used to allow field-cycling experiments to be performed within a superconducting MRI system without major modification to the host system. This approach takes advantages of the well-engineered modern superconducting MR imagers, including advanced RF technology, powerful gradients and optimized pulse sequences. The major advantage of this method is that it

can be readily applied to any static-field MRI without the need of a specialized field-cycling system.

(1.2.9) Gradient and Shim Coils

Only two of the four common MRI magnetic sub-systems have been discussed so far; the main magnet that produces the primary magnetic field, and the RF coil(s) that produce and record the fluctuating fields. Briefly, the other magnetic sub-systems in an MRI will be mentioned. For the MRI system to create two- and three-dimensional objects an additional set of magnets, know as gradients, are required. Gradient coils are specialized electromagnets that produce dynamically controlled magnetic fields that vary linearly along each of the Cartesian axes. They are referred to as the *x*-gradient, *y*-gradient and *z*-gradient. The gradient fields translate the spatial geometry of the sample into either phase or frequency information detected by the RF receive coil. The combination of three gradient coils is sufficient to produce two- or three-dimensional data sets that are reconstructed to form MR images.

Unlike gradient coils, which change rapidly to add frequency and phase encoding in an MRI image, shim coils correct magnetic field inhomogeneities caused when objects with nonzero magnetic susceptibility are placed in the MRI system. Shim coils are typically much weaker than gradients. Often superconducting, they can be adjusted by the MRI machine to optimize the MRI image quality on a patient-to-patient basis.

The main magnet, RF coil, gradients and the shims can all be negatively affected by the additional hardware required for dreMR. In designing dreMR equipment and pulse sequences, care must be taken to minimize interactions between dreMR magnets and other magnet systems. Failure to do so could result in reducing image quality and possible damage to the MRI system.

(1.3) Thesis Overview

The work presented here was performed from 2005 to 2009 in the department of Physics and Astronomy at The University of Western Ontario. The research was a collaborative effort between me, my supervisor Dr. Blaine Chronik, our group's research associates Drs. William Handler and Timothy Scholl and our collaborator Dr. Brian Rutt at Stanford University.

This thesis describes the process of combining the unique features of field-cycled MRI with the availability and performance of superconducting MRI systems, through the application of a dynamically controlled electromagnetic insert coil. In Chapter 2, dreMR is fully presented and the first proof-of-principle dreMR images are shown. The dreMR-subtraction method is introduced, in which two images, created at different magnetic field strengths, are subtracted to produce image maps showing the magnetic field dependence of the relaxation rate within a phantom. The signal-to-noise equation

for the dreMR-subtraction method is derived and the resulting loss in SNR versus gain in specificity is discussed.

In total, two dreMR systems were constructed. The first system is mentioned briefly in Chapter 2 and described in detail Chapter 3. Though this system was satisfactory in demonstrating the dreMR method, it had several limitations. A more powerful, 2nd-generation dreMR system was built next as first step towards a commercially available dreMR system. The improved design is described in Chapter 4. Using a pulse sequence similar to the one described in Chapter 2, MR images were produced at field shifts of 150 mT, demonstrating the magnetic field dependence of the sample relaxation rates.

Chapter 5 introduces the double inversion recovery dreMR sequence. This is the first actual dreMR pulse sequence, capable of creating MR images related to the magnetic field dependence of the sample without post processing of any kind.

Finally, in Chapter 6 the future of dreMR is discussed. We look at possible hardware and software developments and potential applications.

(1.4) References

1. Wood ML, Hardy PA. Proton relaxation enhancement. J Magn Reson Imaging 1993;3(1):149-156.
2. Caravan P. Strategies for increasing the sensitivity of gadolinium based MRI contrast agents. Chem Soc Rev 2006;35(6):512-523.
3. Caravan P, Cloutier NJ, Greenfield MT, McDermid SA, Dunham SU, Bulte JW, Amedio JC, Jr., Looby RJ, Supkowski RM, Horrocks WD, Jr., McMurry TJ, Lauffer RB. The interaction of MS-325 with human serum albumin and its effect on proton relaxation rates. Journal of the American Chemical Society 2002;124(12):3152-3162.
4. Eldredge HB, Spiller M, Chasse JM, Greenwood MT, Caravan P. Species dependence on plasma protein binding and relaxivity of the gadolinium-based MRI contrast agent MS-325. Investigative radiology 2006;41(3):229-243.
5. Overoye-Chan K, Koerner S, Looby RJ, Kolodziej AF, Zech SG, Deng Q, Chasse JM, McMurry TJ, Caravan P. EP-2104R: a fibrin-specific gadolinium-Based MRI contrast agent for detection of thrombus. Journal of the American Chemical Society 2008;130(18):6025-6039.
6. Sosnovik DE, Weissleder R. Emerging concepts in molecular MRI. Current opinion in biotechnology 2007;18(1):4-10.
7. Cowan B. Nuclear Magnetic Resonance. Cambridge: University Press; 1997.
8. E. Mark Haacke ea. Magnetic Resonance Imaging - Physical Principles and Seqence Design: John Wiley & Sons; 1999.
9. Levitt M. Spin Dynamics. Chichester: John Wiley & Sons; 2002.
10. Bottomley PA, Foster TH, Argersinger RE, Pfeifer LM. A review of normal tissue hydrogen NMR relaxation times and relaxation mechanisms from 1-100 MHz: dependence on tissue type, NMR frequency, temperature, species, excision, and age. Med Phys 1984;11(4):425-448.
11. Kimmich .R A, E. Field-cycling NMR relaxometry. Progr Nucl Magn Reson Spectr 2004;44:257 – 320.
12. Mondino F, Filippi P, Magliola U, Duca S. Magnetic resonance relaxometry in Parkinson's disease. Neurol Sci 2002;23 Suppl 2:S87-88.
13. Rinck PA, Fischer HW, Vander Elst L, Van Haverbeke Y, Muller RN. Field-cycling relaxometry: medical applications. Radiology 1988;168(3):843-849.
14. Lopiano L, Fasano M, Giraudo S, Digilio G, Koenig SH, Torre E, Bergamasco B, Aime S. Nuclear magnetic relaxation dispersion profiles of substantia nigra pars compacta in Parkinson's disease patients are consistent with protein aggregation. Neurochem Int 2000;37(4):331-336.

15. Gilbert KM, Handler WB, Scholl TJ, Odegaard JW, Chronik BA. Design of field-cycled magnetic resonance systems for small animal imaging. Phys Med Biol 2006;51(11):2825-2841.
16. Matter NI, Scott GC, Grafendorfer T, Macovski A, Conolly SM. Rapid polarizing field cycling in magnetic resonance imaging. IEEE Trans Med Imaging 2006;25(1):84-93.
17. Ungersma SE, Matter NI, Hardy JW, Venook RD, Macovski A, Conolly SM, Scott GC. Magnetic resonance imaging with T1 dispersion contrast. Magn Reson Med 2006;55(6):1362-1371.
18. Carlson JW, Goldhaber DM, Brito A, Kaufman L. MR relaxometry imaging. Work in progress. Radiology 1992;184(3):635-639.
19. Lurie DJ, Foster MA, Yeung D, Hutchison JM. Design, construction and use of a large-sample field-cycled PEDRI imager. Phys Med Biol 1998;43(7):1877-1886.
20. Lurie DJ, Davies GR, Foster MA, Hutchison JM. Field-cycled PEDRI imaging of free radicals with detection at 450 mT. Magn Reson Imaging 2005;23(2):175-181.

Chapter 2 – Delta relaxation enhanced MR

This chapter is adapted from the published paper: Alford JK, Rutt BK, Scholl TJ, Handler WB, Chronik BA. *Delta relaxation enhanced MR: improving activation-specificity of molecular probes through R1 dispersion imaging*. Magn Reson Med 2009; 61(4): 796-802

(2.1) Introduction

Molecular imaging is the *in-vivo* study and measurement of biological processes at the molecular level (1). Popular molecular imaging modalities include positron emission tomography, single photon emission computed tomography, magnetic resonance imaging, and optical imaging. These modalities rely upon probes or tracers to enhance sites of target molecules or tissues through the complementary processes of accumulation and activation. Accumulation occurs when the local concentration of the probe is increased through metabolic uptake or molecular adhesion and is the principle mechanism for localized image enhancement in nuclear medicine. Many varieties of probe are also activatable, their behavior mediated by interaction with the target molecule. Probes demonstrating activation are variously called "sensing", "smart", or "activatable" probes. For the purposes of this paper, the term activatable will be used. Activatable probes are used in both optical imaging and MRI studies to improve the specificity of the probe (2). Ideally, activatable probes would produce no image enhancement in the inactivated state; however, to date, these probes combined with conventional MRI have shown image intensity enhancement in both inactivated and

activated states, with relatively modest signal intensity ratios between these two states. Herein we describe a means of obtaining increased specificity in magnetic resonance (MR) molecular imaging by utilizing an auxiliary electromagnet to modify the strength of the main magnetic field as a function of time in an otherwise standard MRI scanner. Due to the unique response in relaxivity of activated contrast agents, this technique allows one to specifically identify the location of activated contrast agents within an MR image.

(2.1.1) MRI Contrast Agents

Contrast-enhanced MRI can generally be categorized as either positive or negative contrast. In positive contrast, image intensity increases at sites of MR probe accumulation as a result of the dominating effect of a decreased longitudinal relaxation time (T_1). In negative contrast, image intensity decreases at sites of MR probe accumulation as a result of the dominating effect of a decreased transverse relaxation time (T_2) (3). In this paper, we focus on the application of the variable field technique to activatable T_1 contrast agents only.

The strength of a T_1 contrast agent is best described by its longitudinal relaxivity, r_1 (s^{-1} mM^{-1}); the larger the r_1, the greater its efficiency at increasing the longitudinal relaxation rate ($R_1 = 1 / T_1$) of surrounding tissues and thereby enhancing signal in T_1 weighted MR images. The longitudinal relaxation rate (R_1) of a tissue, which has taken

up a T_1 contrast agent of concentration [*CA*] and relaxivity r_1, can be written as

$$R_1 = R_{1\text{Unenhanced}} + r_1 \cdot [CA].$$

(2.1.2) Relaxivity and Targeted Contrast Agents

The rate of molecular tumbling of a contrast agent in tissue is a factor in determining the relaxivity, r_1 (4). Rapidly tumbling molecules exhibit lower relaxivities (typically < 10 s^{-1} mM^{-1}) that decline gradually with increasing magnetic field strengths above 0.5 T. New activatable contrast agents are designed to bind more specifically and strongly to certain proteins or classes of proteins or other macromolecular or cellular entities. Upon binding, the resulting decreased tumbling rate has been shown to produce a dramatic increase in r_1 at low field strengths (e.g. 0.5 T), with relatively little enhanced relaxivity at higher field strengths (e.g. above 3 T).

Vasovist or MS-325 (Bayer HealthCare Pharmaceuticals, Gadofosveset trisodium) is one particular example of a gadolinium chelate of similar size to conventional gadolinium diethylenetriamine penta-acetic acid (Gd-DTPA); however, by virtue of the addition of a lipophilic diphenylcyclohexyl group, this molecule shows strong non-covalent binding to serum albumin (5,6). In the presence of human serum albumin, the bound form of this agent demonstrates an increase of relaxivity by approximately an order of magnitude at 30 MHz, and approximately four-fold at 60 MHz. The relaxivity curves of Vasovist, in the presence and absence of serum albumin from human and

rabbit, in a buffered saline solution are shown in Figure 2.1 (7). In another instance, the agent Gd-bis-5-HT-DTPA has been developed as a "sensor" of the enzyme myeloperoxidase (8). In the presence of active myeloperoxidase, this agent converts from a monomeric form with minimal protein binding characteristics and relaxivity similar to that of Gd-DTPA, to an oligomeric form with stronger protein binding affinity, leading to enhanced relaxivity. The agent EP-2104R (Epix Pharmaceuticals), is currently in clinical trials (9). This agent will selectively bind to fibrin, a significant component of blood clots (thrombi). Upon binding, EP-2104R demonstrates a 2.3-times increase in relaxivity at 1.5 T.

These three examples of gadolinium-based agents represent the promise of activatable MR contrast agents, but also illustrate a limitation of this class of agents. That is, the activation-induced relaxivity enhancement may be relatively modest, especially at clinical field strengths of 1.5 T or 3 T. As a result, it may be difficult to separate intensity enhancement due to the presence of the activated agent from intensity enhancement due to the presence of larger amounts of the non-activated agent.

To characterize the efficacy of an activatable contrast agent, we define the relaxivity enhancement ratio as the ratio of the activated relaxivity to the inactivated relaxivity. For Vasovist at 1.5 T, the relaxivities in the presence and absence of human albumin are 19 s^{-1} mM^{-1} and 5.2 s^{-1} mM^{-1} respectively, resulting in a relaxivity enhancement ratio of 3.7. From Figure 2.1 it can be seen that the Vasovist relaxivity

enhancement ratio peaks in the vicinity of 0.5 T, and falls quickly for field strengths above that value.

(2.1.3) Delta Relaxation Enhanced Magnetic Resonance

We introduce here a novel method to distinguish between signal intensities produced by tissues containing activated probe from all other sources of signal intensity, which we have termed delta relaxation enhanced MR (dreMR) (10). This approach finds its roots in field-cycling relaxometry imaging methods used by Carlson *et al.* (11) as a means to differentiate biological tissues. Carlson outfitted a 64 mT whole-body MR with a pulsed electromagnet insert in order to modulate the strength of the main magnetic field during an imaging experiment. He was able to show that at low magnetic field strengths the R_1 profiles of biological tissues contained features such as cross relaxation peaks and quadruple dips (12), which could permit differentiation between healthy and pathological tissues.

While Carlson used low-field R_1 field variations to identify biological tissues, our approach utilizes the relative lack of R_1 field variation (13,14) at higher field strengths as a means to reject signal from both unenhanced tissues and tissues enhanced by inactivated probe. Defining R_1' and r_1' as the partial derivatives of R_1 and r_1 with respect to B_0 results in $R_1' = R_{1\text{Unenhanced}}' + r_1' * [CA]$. Applying the approximation that $R_{1\text{Unenhanced}}' \approx 0$ for fields above 1.0 T, results in the expression $R_1' \approx r_1' * [CA]$. This

simple relation shows that the rate of change of the longitudinal relaxation rate (R_1') depends almost exclusively on the rate of change of probe relaxivity (r_1') with magnetic field. While activated probes demonstrate high values of r_1', inactivated probes have r_1' values close to zero (Figure 2.1). For Vasovist, the relaxivity *slope* enhancement ratio (ratio of activated r_1' to inactivated r_1') is 90 at 1.5 T. This represents a 25-fold increase over the absolute relaxivity enhancement ratio of 3.7 mentioned above. The high specificity of dreMR enhancement is not specific to Vasovist but would apply to any T_1 contrast agents that undergo binding to large molecules (15).

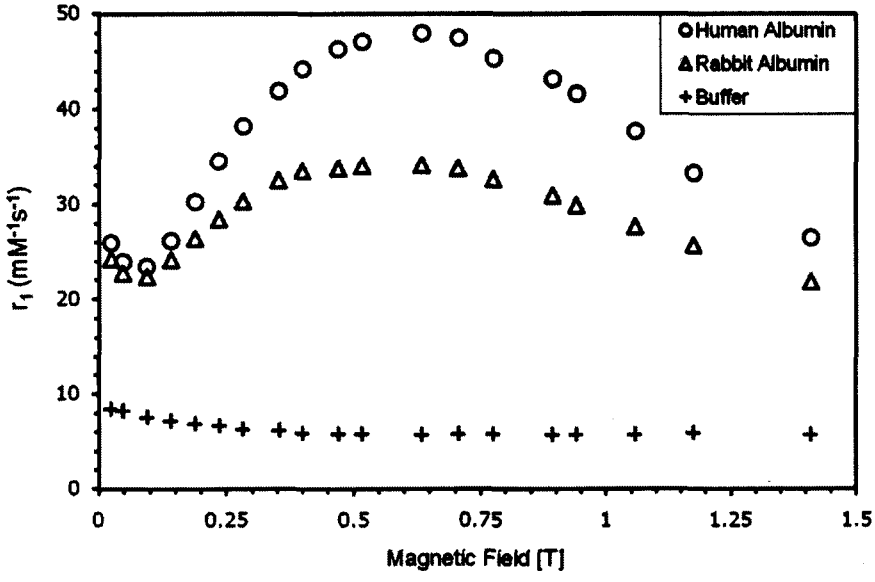

Figure 2.1 Relaxivity curves of Vasovist (MS-325). Relaxivity as a function of field strength for 0.1 mM Vasovist (MS-325) in PBS (NaCl 0.138M, KCl 0.0027M, pH 7.4 at 25 °C) alone (+) or in PBS plus 4.5% (wt/vol) human (○) or rabbit (Δ) serum albumin at 35°C, PBS. The relaxivity of the bound agent is highly dependent on the strength of the applied magnetic field. In contrast, the relaxivity of the unbound agent demonstrates very little field dependence over that same range in water.

Transforming R_1' into image contrast requires the ability to dynamically vary the strength of the main magnetic field in an MR system. Access to such platforms is limited to a handful of sites worldwide (16-18); however, an alternative approach involves outfitting clinical MR systems with custom electromagnetic coils to enable variable field operation. The magnetic field shift need only be applied during longitudinal relaxation periods where extremely high stability and homogeneity are not necessary. The main field would not be altered during actual signal acquisition or any radiofrequency pulse application. This means that the normal radiofrequency transmit/receive chain can be used without modification. In the following paragraphs we present the theory and first experimental demonstration of dreMR, using a small-bore actively-shielded field-cycling electromagnet within an otherwise conventional 1.5 T clinical MR scanner.

(2.2) Theory

(2.2.1) dreMR Image Subtraction

There are multiple methods that can be employed to generate dreMR contrast. The simplest method involves the weighted subtraction of two T_1 weighted images, each image acquired with a slightly different sequence. These sequences, referred to as the T_{1+} and T_{1-} sequences, both resemble T_1 weighted sequences; however, in the T_{1+} sequence a field increasing ΔB pulse is applied during longitudinal relaxation, while in the T_{1-} sequence a field decreasing ΔB pulse is used. In Figure 2.2 the T_{1+} and T_{1-}

Transforming R_1' into image contrast requires the ability to dynamically vary the strength of the main magnetic field in an MR system. Access to such platforms is limited to a handful of sites worldwide (16-18); however, an alternative approach involves outfitting clinical MR systems with custom electromagnetic coils to enable variable field operation. The magnetic field shift need only be applied during longitudinal relaxation periods where extremely high stability and homogeneity are not necessary. The main field would not be altered during actual signal acquisition or any radiofrequency pulse application. This means that the normal radiofrequency transmit/receive chain can be used without modification. In the following paragraphs we present the theory and first experimental demonstration of dreMR, using a small-bore actively-shielded field-cycling electromagnet within an otherwise conventional 1.5 T clinical MR scanner.

(2.2) Theory

(2.2.1) dreMR Image Subtraction

There are multiple methods that can be employed to generate dreMR contrast. The simplest method involves the weighted subtraction of two T_1 weighted images, each image acquired with a slightly different sequence. These sequences, referred to as the T_{1+} and T_{1-} sequences, both resemble T_1 weighted sequences; however, in the T_{1+} sequence a field increasing ΔB pulse is applied during longitudinal relaxation, while in the T_{1-} sequence a field decreasing ΔB pulse is used. In Figure 2.2 the T_{1+} and T_{1-}

sequences are shown. Each sequence contains a preparatory module where the static magnetic field strength (B_0) is either increased or decreased by an amount ΔB, as well as a self-contained acquisition module, which may be a conventional imaging sequence such as gradient recalled echo, spin echo, fast spin echo, etc. In this example a spin-echo acquisition module is shown. On the final line of Figure 2.2 the longitudinal magnetization of two theoretical tissues is shown. The R_1 rate of the tissue represented by the solid curve is nearly independent of magnetic field strength and therefore relaxes identically for both the T_{1-} and T_{1+} sequences. However, the R_1 rate of the tissue represented by the dashed curve is highly dependent upon the strength of the magnetic field; increasing at lower field strengths and decreasing at higher field strengths. Subtraction of the images produced by the T_{1-} and T_{1+} sequences would result in an image where the only intensity would be due to the field dependent tissue. The other tissue would be completely suppressed.

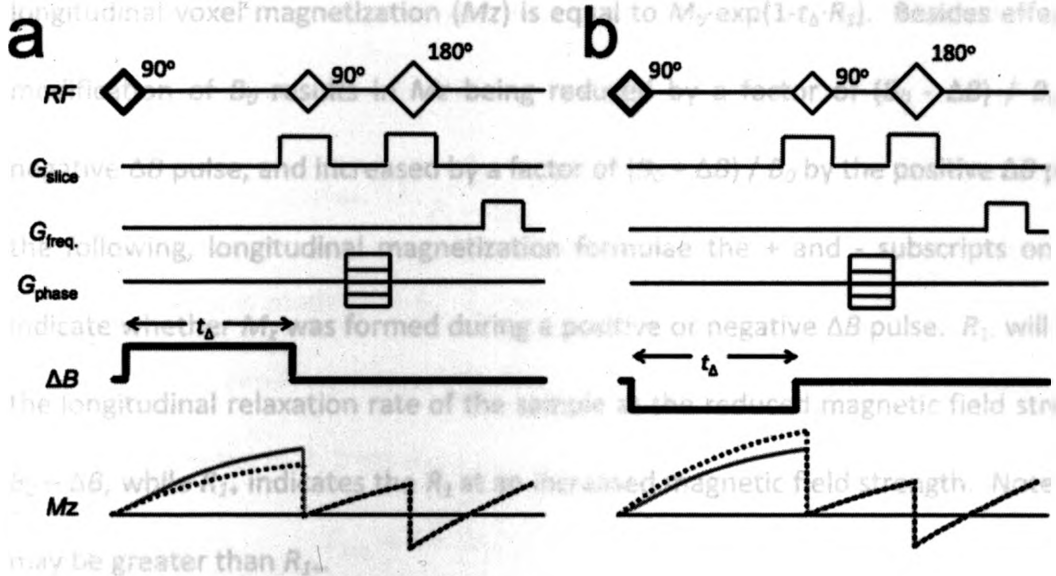

Figure 2.2. Modified spin-echo pulse sequence. Detection of T_1 field dependence requires the ability to manipulate the main field strength. (a) The T_1+ sequence and (b) the T_1- sequence are spin-echo T_1 weighted sequences where a ΔB pulse of duration t_Δ has been used to modify the strength of the static B_0 field. On the bottom line the longitudinal magnetization of two theoretical tissues is shown. The dashed line represents the magnetization of a tissue having a strongly field-dependent R_1 value, while the solid line represents the magnetization of a tissue without any significant field dependence.

The following analytic treatment is provided to help describe this method. To simplify the analytic treatment it is assumed that each preparatory ΔB module begins with a saturation radiofrequency pulse to eliminate any preexisting longitudinal magnetization; however, other initialization states could be used in a similar analysis. The effect of finite ramping times for the ΔB pulse will be ignored. Starting at Curie's Law, the steady state longitudinal magnetization (M_0) is proportional to the amplitude of the applied magnetic field. Following the completion of a ΔB pulse of duration t_Δ the

longitudinal voxel magnetization (Mz) is equal to $M_0 \cdot \exp(1-t_\Delta \cdot R_1)$. Besides effecting R_1, modification of B_0 results in Mz being reduced by a factor of $(B_0 - \Delta B) / B_0$ by the negative ΔB pulse, and increased by a factor of $(B_0 + \Delta B) / B_0$ by the positive ΔB pulse. In the following, longitudinal magnetization formulae the + and - subscripts on M_z will indicate whether M_z was formed during a positive or negative ΔB pulse. R_{1-} will indicate the longitudinal relaxation rate of the sample at the reduced magnetic field strength of $B_0 - \Delta B$, while R_{1+} indicates the R_1 at an increased magnetic field strength. Note that R_{1-} may be greater than R_{1+}.

$$M_{z-} = M_0 \cdot \frac{B_0 - \Delta B}{B_0}\left[1 - \exp\left(-t_\Delta \cdot R_{1-}\right)\right] \qquad [2.1]$$

$$M_{z+} = M_0 \cdot \frac{B_0 + \Delta B}{B_0}\left[1 - \exp\left(-t_\Delta \cdot R_{1+}\right)\right] \qquad [2.2]$$

Image voxel intensity is determined by the combined actions of the acquisition module, detector hardware, and MR console software. For simplicity, it will be assumed that the acquired image intensity is a product of the actual voxel magnetization (M_z), and a single positionally dependent term, k, that incorporates proton density, radiofrequency coil homogeneity, transverse relaxation time, and any other scaling factors. The resulting image intensity (absolute value) in each pixel $I(x, y)$ is then related to voxel magnetization: $I(x, y) = k(x, y, \mathbf{r}) \cdot M_z(\mathbf{r})$. Forming the dreMR image requires taking the normalized difference of the I_- and I_+ images. Due to the different equilibrium

magnetization introduced by the magnetic field shifts, the image magnitudes I_- and I_+ must be normalized prior to subtraction,

$$I_{Sub.} = I_- \frac{B_0}{B_0 - \Delta B} - I_+ \frac{B_0}{B_0 + \Delta B} \qquad [2.3]$$

If the assumption is made that R_1' is constant in the vicinity of B_0 then it is possible to approximate the resulting image intensity by the following expression, wherein ΔR_1 is the absolute change in R_1 from B_0 to $B_0 \pm \Delta B$:

$$I_{\text{Sub.}} \approx 2k \cdot M_0 \cdot \sinh(t_\Delta \cdot \Delta R_1) \cdot \exp(-t_\Delta \cdot R_1). \qquad [2.4]$$

There are two non-linear terms in Eq. 2.4. The hyperbolic sine and exponential decay functions. The hyperbolic sine term, though non-linear, is responsible for the distinctive contrast produced by this method. It indicates that difference in intensity between voxels in the final dreMR image will be related to the R_1' values of those voxels. Because of the unique nature of dreMR, direct comparison of tissue contrasts produced by this method to other MR methods can be made only in specific instances.

The exponential decay function unfortunately results in loss of contrast when the longitudinal relaxation time t_Δ is set too long and the voxel magnetizations of the I_- and I_+ images begin to saturate. This is comparable to using a T_R much longer than T_1 when taking a T_1 weighted image. If t_Δ is chosen so that the maximum product of $t_\Delta \cdot R_1$ is less than 0.2, then maximum shading is limited to at most 20 percent. In the same way, if t_Δ is chosen so that the maximum product of $t_\Delta \cdot \Delta R_1$ is less than 0.5 then nonlinearity effects are limited below 5%. Equation 2.5a shows that with the appropriate choice of

t_Δ image intensity becomes linear with ΔR_1. Equation 2.5b expresses the result more explicitly with ΔR_1 replaced by the product of R_1' and ΔB; that is, the slope of R_1 multiplied by the strength of the magnetic field shift.

$$I_{\text{Sub.}} \approx 2k \cdot M_0 \cdot t_\Delta \cdot \Delta R_1 \qquad [2.5a]$$

$$I_{\text{Sub.}} \approx 2k \cdot M_0 \cdot t_\Delta \cdot \Delta B \cdot R_1' \qquad [2.5b]$$

This is the first and simplest implementation of dreMR. With this implementation, it is possible to produce image intensities that depend on the change in R_1 rather than in R_1 itself. Activatable contrast agents of the types described in the Introduction all produce major changes in R_1' upon activation, even if the enhancement in R_1 is much smaller. This is the essence of dreMR and illustrates its potential application to the specific imaging of activatable MR probes.

It is necessary to understand the reduction in signal to noise ratio (SNR) for this new method. Because of the restrictions placed previously, that is $t_\Delta \cdot R_1 < 0.2$, the SNR of the constituent images, I_- and I_+, after normalization can be approximated as $k \cdot M_0 \cdot t_\Delta \cdot R_1/\sigma$ where σ is uncertainty in the images after normalization. Dividing Eq. 2.5b by σ gives the SNR of the dreMR image. This result can be written in terms of the SNR of the source images as:

$$\text{SNR}_{\text{Sub.}} \approx \sqrt{2} \cdot \Delta B \cdot R_1' / R_1 \cdot SNR \qquad [2.6]$$

Equation 2.6 again involves an approximation; it is assumed the magnetic field shifts about B_0 are small enough such that the uncertainties of the I_- and I_+ images are

identical. When the field shifts are larger, the SNR equation must take into account the different uncertainties in each image.

For a $R_1' \cdot \Delta B$ (ΔR_1) of 1 s^{-1} and an R_1 of 10 s^{-1} the SNR of the dreMR image drops to 14% of the SNR of the source image. Beyond simply gauging the loss in SNR, Eq. 2.6 illustrates that the maximum SNR would be produced by contrast agents that demonstrate a sharp change in r_1 (large r_1') for a small value of r_1. Evaluating the r_1'/r_1 of a molecular probe may provide a basis for determining which molecular probes would benefit from dreMR contrast.

This derivation has outlined the most basic method to produce dreMR contrast. Other more complicated methods could certainly be applied. A double subtraction method for example could utilize several inversion pulses as well as several ΔB pulses to achieve dreMR contrast without subtraction.

(2.3) Materials and Methods

To demonstrate the feasibility of dreMR imaging, the agent Vasovist (MS-325) was imaged in the presence and absence of rabbit serum albumin (RSA). As shown in Figure 2.1, Vasovist preferentially binds to albumin, producing moderate enhancement in the inactivated state and higher enhancement in the activated state. The particular choice of agent/protein pair was based by the availability of the agent and its well-documented relaxivity mechanisms, rather than any specific clinical or research interest in albumin.

(2.3.1) Phantom

An MRI phantom (see Figure 2.3a) was constructed that held two columns of six rows of glass tubes; each tube 3 cm in length with a 0.4 mL capacity. The samples tubes in the left column were filled with 0.01 M phosphate buffered saline (PBS) (NaCl 0.138M, KCl 0.0027M, pH 7.4 at 25 °C). The right column of sample tubes held a solute of rabbit serum albumin (Sigma-Aldrich, batch 104K7560, agarose gel electrophoresis) in PBS. The albumin, purchased as a lyophilized powder, was dissolved in PBS at the biologically significant concentration of 4.5% weight to volume ratio, resulting in 0.67mM concentration. Vasovist (0.25 mmol/mL) was added in equal concentration to both columns to achieve sample concentrations of 0, 10, 20, 40, 80 and 160 μM as a function of descending rows.

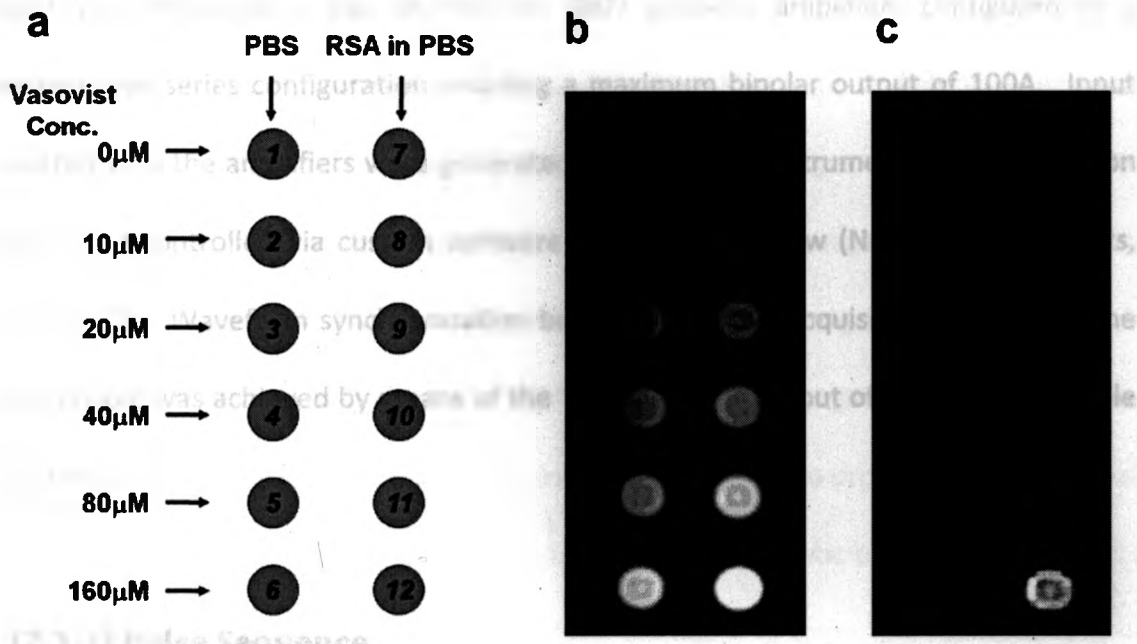

Figure 2.3. Phantom and MRI images. a) The arrangement of samples in the phantom: The left column (samples 1 to 6) contains PBS while the right column (samples 7 to 12) contains rabbit serum albumin diluted in PBS buffer at 4.5% weight/volume. Concentrations of Vasovist are given for each row, ranging from 0 to 160 μM. b) A T_1 weighted image of the samples. Since Vasovist will produce enhancement, either free or bound to albumin, the intensities of both columns increase with Vasovist concentration (downward). c) The dreMR image for the same samples. The left column of samples exhibit reduced signal while the samples on the right side, containing albumin, continue to show an increased signal with Vasovist concentration.

(2.3.2) Hardware

Imaging was performed on a (General Electric Healthcare) Sigma LX 1.5 T clinical MRI platform, equipped with a custom-built actively shielded B_0 insert coil (19). The insert, designed to generate ± ΔB pulses, had an efficiency of 0.7 mT/A, weighed approximately 150 kg and was designed to facilitate the imaging of animals as large as rabbits. The

insert was driven by a pair of Techron 8607 gradient amplifiers configured in a master/slave series configuration enabling a maximum bipolar output of 100A. Input waveforms to the amplifiers were generated by a National Instruments data acquisition device and controlled via custom software written in LabView (National Instruments, version 8.2). Waveform synchronization between the data acquisition device and the MRI console was achieved by means of the 'scope trigger' output of the system console electronics.

(2.3.3) Pulse Sequence

The following spin-echo pulse sequence parameters were used for all images that were combined to produce the final dreMR image: 150 ms pulse repetition time, 10 ms echo time, 31 kHz bandwidth, 8 cm field of view and 10 mm slice thickness. The scan time was 24s for each image. For each row of *k*-space, 70 mT ΔB pulses were applied for 100-ms intervals. The ΔB pulses were timed to end 10 ms prior to image acquisition to allow both the magnetic field of the MR and amplifiers time to stabilize. This sequence differed slightly from the sequence shown in Figure 2.2; it lacked the preparatory radio frequency pulse. Because the duration of the ΔB pulse was significant compared to the repeat time this resulted in only a small deviation from the ideal. By using a 'built-in' pulse sequence, rather than a custom sequence, it would be clear that the resulting contrasts were due to dreMR and not an error in the pulse sequence.

For T_{1+} images the magnetic field was increased by 70 mT during the relaxation portion of the pulse sequence. Likewise for T_{1-} images the magnetic field was decreased by the same amount. Ten pairs of T_{1+} and T_{1-} weighted images were acquired for the samples held at 21 °C. Acquisitions of T_{1+} and T_{1-} enhanced images were interleaved to minimize heating of the amplifiers. The positively enhanced images were then averaged into a single dataset, as were the negatively enhanced images. The resulting two datasets were normalized and the absolute difference taken to produce contrast related to the magnetic field dependence of R_1. Unlike in the theoretic treatment a saturation pulse was not applied prior to the B_0 pulse. Standard T_1 weighted spin echo images using the same pulse sequence parameters were acquired for comparison.

(2.4) Results

Figure 2.3 shows the standard T_1 weighted spin-echo image of the samples. As expected, the intensity of both columns increased from top to bottom with concentration of Vasovist. The measured average intensity within each sample is plotted in Figure 2.4a. The error bar on each data point indicates the standard deviation of voxel intensity throughout the corresponding sample. Both sets of samples, albumin solution and PBS-only, demonstrated significant dependence on Vasovist concentration. Because the range of intensities of the albumin samples (▲) were not clearly separated from those of the PBS-only samples (●) but in fact were appreciably overlapped, it is

clear that without prior knowledge of Vasovist concentrations, it would not be possible to differentiate the albumin-containing sample from PBS-only samples based on T_1 weighted image intensity alone.

Figure 2.3c illustrates the absolute difference of the ± ΔB datasets. The figure shows the entire dynamic range without thresholding. The average intensity from each of the samples is plotted in Figure 2.4b. The standard deviation of voxel intensities within each sample is again expressed as an error bar. While the image intensity of albumin samples continued to demonstrate dependence on Vasovist concentration, the PBS-only samples where significantly suppressed. The intensities of all PBS-only samples were suppressed well below the intensity of the weakest albumin-loaded sample, which had only a 10μM Vasovist concentration. Thus, a substantially increased specificity to albumin was obtained through dreMR imaging.

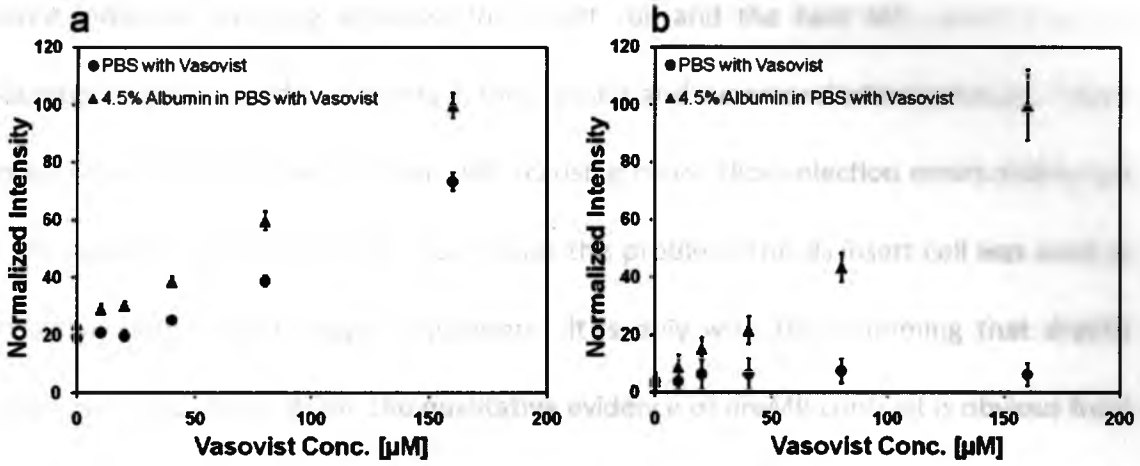

Figure 2.4. Sample intensities from MRI and dreMR images. a) Sample intensities of the T_1 weighted image are plotted versus Vasovist concentration. As expected with rabbit albumin (▲) samples are enhanced more than the phosphate buffered saline (PBS) (●) samples at the same concentration; however without *a priori* knowledge of Vasovist concentrations it would not be possible to differentiate albumin-containing samples from pure PBS samples. b) Normalized intensities from the dreMR method are shown. Notice the drastic suppression of intensity for the samples containing only PBS and Vasovist.

Intensity variations in the dreMR image were seen to increase by a factor of 2.5 times those of the T_1 weighted image as indicated by the larger error bars in Figure 2.4b compared to Figure 2.4a. This increase was due to the combined effects of SNR loss and introduction of subtraction artefacts. Subtraction artefacts appear as a mottling across the samples and are due to instabilities in the B_0 field during image acquisition; instabilities most likely introduced by rapid switching of the B_0 insert coil. Subtraction artefacts were localized to positions having significant image intensity in the constituent images whereas noise increased across the entire image. Even with active shielding,

minor inductive coupling between the insert coil and the host MR system has the potential to produce eddy currents in the cryostat and superconductive windings. These eddy currents destabilize the main field, causing minor slice selection errors and errors in the radiofrequency tip angle. To counter this problem, the B_0 insert coil was used as an active shim during image acquisition. It is only with this shimming that dreMR images were possible. While the qualitative evidence of dreMR contrast is obvious from Figure 2.3c, more quantifiable measurements will require additional improvements in the stability of the magnetic field.

(2.5) Discussion

dreMR imaging is a method for producing image contrast proportional to ΔR_1, or more explicitly, the product of R_1' and ΔB where ΔB has been created by a field-cycling insert magnet. One primary application is the significant improvement in specificity of gadolinium based agents that undergo targeted binding to larger molecules or proteins (e.g. EP-2104R and Vasovist). The appeal of dreMR contrast is that it does not require further engineering of contrast agents to obtain specificity but can be applied to preexisting agents immediately. Furthermore, it may also be possible to design contrast agents specific for dreMR imaging. Such agents would demonstrate extremely high r_1 slope when activated and little or ideally no r_1 slope when inactivated.

The simplest source of dreMR contrast is the weighted subtraction method, where the difference is taken of two T_1 weighted images, each having received a different field strength during the longitudinal relaxation period. The signal equation for this sequence was shown to be nearly linear with the difference in R_1 between two field strengths. This method is prone to image shading that would occur in samples with high R_1 due to the image shading term $\exp(-t_\Delta \cdot R_1)$. This shading can be constrained by shortening t_Δ, the duration of the ΔB pulse, at the expense of SNR.

(2.6) Conclusions

A proof-of-principle experiment was performed that demonstrates the specificity of Vasovist to albumin could be greatly improved using dreMR contrast over conventional T_1 weighted contrast. As expected, the cost of increased specificity was a decrease in SNR as well as the appearance of a subtraction artefact. The SNR equation for the subtraction sequence had indicated a loss in SNR, but also showed that SNR could be improved by increasing ΔB, the intensity of the magnetic field shift. Subtraction artefacts are reduced by decreasing the inductive coupling between the insert and the host MR system. New insert coil designs that will permit magnetic field shifts in clinical MR systems up to 750 mT while further reducing coupling between the insert and the host system are under development.

(2.7) References

1. Weissleder R, Mahmood U. Molecular imaging. Radiology 2001;219(2):316-333.
2. Nahrendorf M, Sosnovik DE, Weissleder R. MR-optical imaging of cardiovascular molecular targets. Basic research in cardiology 2008;103(2):87-94.
3. Hendrick RE, Haacke EM. Basic physics of MR contrast agents and maximization of image contrast. J Magn Reson Imaging 1993;3(1):137-148.
4. Wood ML, Hardy PA. Proton relaxation enhancement. J Magn Reson Imaging 1993;3(1):149-156.
5. Caravan P, Cloutier NJ, Greenfield MT, McDermid SA, Dunham SU, Bulte JW, Amedio JC, Jr., Looby RJ, Supkowski RM, Horrocks WD, Jr., McMurry TJ, Lauffer RB. The interaction of MS-325 with human serum albumin and its effect on proton relaxation rates. Journal of the American Chemical Society 2002;124(12):3152-3162.
6. Henrotte V, Vander Elst L, Laurent S, Muller RN. Comprehensive investigation of the non-covalent binding of MRI contrast agents with human serum albumin. J Biol Inorg Chem 2007;12(6):929-937.
7. Eldredge HB, Spiller M, Chasse JM, Greenwood MT, Caravan P. Species dependence on plasma protein binding and relaxivity of the gadolinium-based MRI contrast agent MS-325. Investigative radiology 2006;41(3):229-243.
8. Nahrendorf M, Sosnovik D, Chen JW, Panizzi P, Figueiredo JL, Aikawa E, Libby P, Swirski FK, Weissleder R. Activatable magnetic resonance imaging agent reports myeloperoxidase activity in healing infarcts and noninvasively detects the antiinflammatory effects of atorvastatin on ischemia-reperfusion injury. Circulation 2008;117(9):1153-1160.
9. Overoye-Chan K, Koerner S, Looby RJ, Kolodziej AF, Zech SG, Deng Q, Chasse JM, McMurry TJ, Caravan P. EP-2104R: a fibrin-specific gadolinium-Based MRI contrast agent for detection of thrombus. Journal of the American Chemical Society 2008;130(18):6025-6039.
10. Alford JK. Delta relaxation enhanced MR (dreMR): Theory of T1-slope weighted contrast. ISMRM. Toronto, Canada; 2008.
11. Carlson JW, Goldhaber DM, Brito A, Kaufman L. MR relaxometry imaging. Work in progress. Radiology 1992;184(3):635-639.
12. Ungersma SE, Matter NI, Hardy JW, Venook RD, Macovski A, Conolly SM, Scott GC. Magnetic resonance imaging with T1 dispersion contrast. Magn Reson Med 2006;55(6):1362-1371.
13. Bottomley PA, Foster TH, Argersinger RE, Pfeifer LM. A review of normal tissue hydrogen NMR relaxation times and relaxation mechanisms from 1-100 MHz: dependence on tissue type, NMR frequency, temperature, species, excision, and age. Med Phys 1984;11(4):425-448.

14. Henriksen O, de Certaines JD, Spisni A, Cortsen M, Muller RN, Ring PB. In vivo field dependence of proton relaxation times in human brain, liver and skeletal muscle: a multicenter study. Magn Reson Imaging 1993;11(6):851-856.
15. Zhou X, Caravan P, Clarkson RB, Westlund PO. On the philosophy of optimizing contrast agents. An analysis of 1H NMRD profiles and ESR lineshapes of the Gd(III)complex MS-325+HSA. J Magn Reson 2004;167(1):147-160.
16. Gilbert KM, Handler WB, Scholl TJ, Odegaard JW, Chronik BA. Design of field-cycled magnetic resonance systems for small animal imaging. Phys Med Biol 2006;51(11):2825-2841.
17. Matter NI, Scott GC, Grafendorfer T, Macovski A, Conolly SM. Rapid polarizing field cycling in magnetic resonance imaging. IEEE Trans Med Imaging 2006;25(1):84-93.
18. Lurie DJ, Foster MA, Yeung D, Hutchison JM. Design, construction and use of a large-sample field-cycled PEDRI imager. Phys Med Biol 1998;43(7):1877-1886.
19. Alford J. From static to dynamic: Construction of an actively shielded B_0 coil for field-cycled imaging with clinical MR platforms. ISMRM. Toronto, Canada; 2008.

Chapter 3 – Design and construction of a B_0 coil

This chapter is adapted from the published paper: Alford JK, Scholl TJ, Handler WB, Chronik BA. *Design and construction of a prototype high-power B_0 insert coil for field-cycled imaging in superconducting MRI systems*. Concepts in Magnetic Resonance Part B: Magnetic Resonance Engineering 2009; 35B(1):1-10.

(3.1) Introduction

B_0 insert coils are auxiliary magnets that are inserted into the bore (imaging region) of clinical MR systems to dynamically manipulate the internal magnetic field to be stronger or weaker than the static field of the MR imager. Such devices have been previously employed as a means to differentiate tissue types in low-field MR imagers (1), but with limited success. These approaches involved varying the strength of the magnetic field over a series of images in order to build up a longitudinal relaxation time (T_1) versus B_0 profile for each image voxel. Analysis of these "T_1-profiles" was then used to assist in tissue identification. This method is time consuming; requiring many T_1-weighted images to produce the T_1-profile and works best when applied at low (< 100 mT) field strengths. At higher magnetic field strengths, T_1-profiles become flat (2) losing many of the interesting identifiable features such as cross-relaxation peaks (3), which could permit differentiation between healthy and pathological tissues. Due in part to the

steady progression towards larger magnetic fields, T_1-profile tissue identification has never transitioned from scientific investigation to clinical practice.

(3.1.1) Field-cycling with contrast agents

Tissue identification based on field-cycled (variable field) magnetic resonance imaging (4-6) can be improved by a new technique (7,8). Although similar to other field-cycling methods, this new technique contains some important distinctions. It combines the concept of field-cycling tissue identification with the use of molecule-specific contrast agents (9-11). These agents produce a selective tissue enhancement by binding to proteins or other large constituent molecules of a particular tissue of interest. Often these agents are used in non-field-cycled MRI applications, but difficulties arise in differentiating the source of image enhancements as either being caused by bound contrast agent or unbound contrast agent. Through the combination of field-cycled imaging and molecularly specific contrast agents comes the ability to selectively enhance a single tissue type while effectively suppressing all other sources of image intensity. Rather than exploiting features of the T_1-profile to differentiate tissues at low field strengths, as would be done with traditional field-cycling techniques, this method utilizes the flatness of the T_1-profile with field strength, common to all biological tissues at high field strengths, as a means to suppress image intensity from biological tissues as well as biological tissues containing unbound contrast agents. The source of this specificity is the slope of the T_1-profile: While both bound (activated) and unbound

(inactivated) molecular probes will change the T_1-value of surrounding tissue, only bound agents will significantly alter the slope of their profile. Therefore by using the *slope* of the T_1-curve as a measure of contrast agent activation rather than a single T_1-value at particular field strength, it becomes possible to distinguish between MRI signal due to bound and unbound agent.

(3.1.2) Field cycling on superconducting MRI platforms

Translating T_1-slope into MR image contrast requires the ability to vary the magnetic field strength of a magnetic resonance imaging system. Rather than using a true variable-field MRI platform (12), and thus limiting the applicability of this research to a few rare sites worldwide, it is expedient to use an auxiliary insertable magnet specifically designed for variable field MRI in a static-field superconducting MRI system. These "insert coils" produce strong B_0 field shifts that modify the strength of the magnetic field during the longitudinal relaxation portion of the pulse sequence. With this approach, the magnetic field shift is only applied during longitudinal relaxation periods where stability and homogeneity are less important, and not during image acquisition. This is significant since the original radio frequency transmit/receive hardware can be used without alteration.

This paper details the various steps necessary to design and construct an electromagnetic insert to perform field-cycling experiments in clinical MRI systems. Initial results are described for a prototype field-cycling insert coil, which was used to

produce 0.07-T-field shifts in a 1.5-T clinical superconducting MRI system. Finally the results of a field-cycled MRI experiment are shown, which demonstrate the ability of field-cycled MRI to produce unique contrast in molecular imaging experiments.

(3.2) Materials and Methods

For an auxiliary insert coil to produce the required magnetic field shifts specific design criteria must be met. These considerations include; torques and forces, magnetic field efficiency, inductance and ramping time, insert cooling and inductive coupling.

(3.2.1) Torque and force

The insert should be designed in such a manner that it experiences little or no net force or torque even if misaligned within the host system. With a high-power insert, the torque can be strong enough to cause injury and/or extensive damage. The addition of an active shield to a solenoid can effectively reduce the net torque even when the insert is incorrectly oriented.

(3.2.2) Field efficiency

The range over which the T_1-profile can be measured directly depends on the maximum strength of the B_0 insert; therefore the magnet should be designed so that B_0 shift should be as large as possible. For solenoidal insert coils this suggests for a given input

power, that the inner diameter of the magnet be as small as possible. It has long been shown that most power-efficient solenoids are designed so that the ratio of outer radius to inner radius is three and the ratio of length to inner radius is four (13). Unfortunately, the maximum achievable efficiency is typically limited by other realities such as cost, heat dissipation and available cooling, insert coil weight and size to name a few.

(3.2.3) Inductance and ramp time

The B_0 insert must be capable of rapidly producing a significant field shift, ΔB, of sufficient duration to produce image contrast and then be ramped down in a time shorter or comparable to T_1 of the sample. This requires that the inductance of the system be kept as low as possible to minimize ramping time. The time required, to ramp an insert of inductance, L, and resistance, R, to a current of, I, using a supply with a maximum voltage V_{max} is given by $\Delta T_{ramp} = -L/R \cdot \ln\left(1 - I \cdot R/V_{max}\right)$.

(3.2.4) Insert cooling

The power deposited in the insert coil increases as the square of the field strength. Therefore, it is the ability to cool the magnet that will ultimately determine the maximum field strength that can be achieved. And whereas additional power may be added later by changing to a superior supply, it is difficult to increase the rate of cooling

after construction is complete. When insufficient cooling exists either the duty cycle or the maximum field of the insert must be reduced. Since both options reduce the signal-to-noise ratio (SNR) provision for adequate cooling and careful choice of materials for construction must always be engineered into the magnet design.

(3.2.5) Inductive coupling

Inductive coupling between a B_0 insert coil and the host MR imaging system is an important consideration since this interaction between these two magnets could lead to serious degradation of image quality. Fast ramping of the insert coil field results in eddy currents (14) in the cold bore of the MRI reducing the stability of the main magnetic field and resulting in an increase in artefact and decrease in signal. This inductive coupling can be reduced by choosing magnet geometries that have minimal coupling between insert and host. For magnet designs that inherently couple with the host MRI, such as solenoids, an active shield may be added. An active shield is a set of counter-windings that lower the inductive coupling and magnet self-inductance by reducing the magnitude of the insert coil's fringe field.

(3.2.6) Shield design

The actively shielded B_0 solenoid described here is an insertable electromagnet consisting of a primary solenoid and a concentric single radial layer of predominantly

counter-windings at a larger radius forming the active shield. The role of the shield is to limit the interactions between the primary solenoid and the MRI host system.

For this insert coil, a simple target-field method (15) was used to generate a shield winding that would reduce the primary magnetic field outside the physical extent of the insert. This method determines the current required to produce a particular magnetic field that has been specified at a number of target points. To design a shield that would effectively remove the fringe magnetic field beyond the insert coil, the fringe magnetic field due to the primary magnet was calculated along the outer edge of the insert. From these discrete target points, a cylindrical current density was calculated which to allowed the shield to cancel the fringe magnetic field of the primary. Current density is the current per wire divided by the separation distance of neighboring wires. Once the necessary current density was determined, it was converted into a discrete wire pattern in which each wire carried a current identical to that of the primary solenoid. By electrically connecting the shield winding in series to the primary solenoid so that the external fields of these magnets were in opposition, the magnetic field outside the insert assembly was largely eliminated.

(3.2.7) Construction

The primary magnet is composed of an epoxy-reinforced solenoid wound with #4 American wire gauge, square cross-section, magnet wire. The coil's inner diameter, outer diameter and length were 19, 25 and 27 cm respectably. The primary magnet was

built in two sub-coils, each consisting of 6 radial layers of 25 axial windings. A gap of 25 mm was added between the sub-coils to increase the homogeneity of the magnetic field to 2%.

The shield employed 108 turns of #7 AWG-equivalent Litz magnet wire wound around a 36-cm-diameter Ultem (amorphous polyetherimide) polymer birdcage-like form as illustrated in Figure 3.1. The Litz wire has a rectangular cross-section of 8 mm by 2 mm. The Litz wire was wound into 2 mm wide by 4mm deep slots that had been milled into the Ultem birdcage at locations specified by the design algorithm.

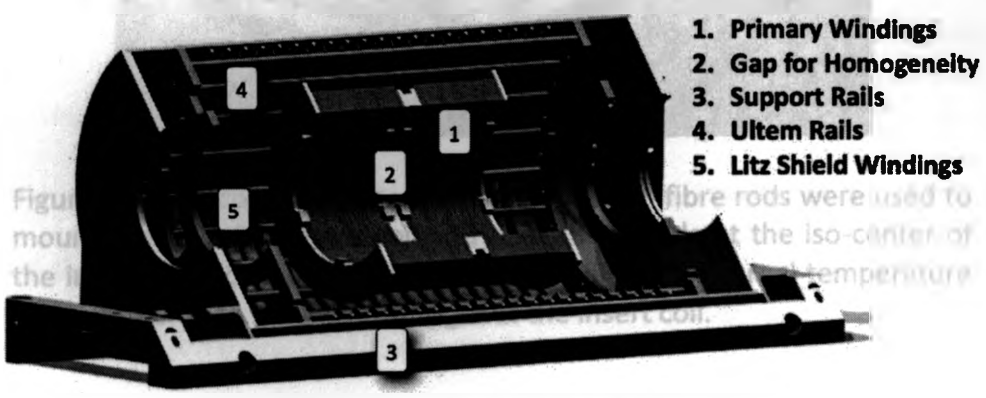

Figure 3.1. CAD drawing of dreMR coil. A computer aided design or CAD drawing of the insert system is shown. Note, the shield windings in this diagram are depicted as being equally spaced for convenience of illustration only.

Together, both primary and shield were cooled with approximately 100 m of 6.35-mm-OD thin-wall Teflon tubing wound in close proximity to the inner and outer surfaces of the magnets. The entire insert was potted in 60 litres of thermally

conductive epoxy resin (part # 51-3100, Epoxies Etc.) resulting in a total system weight of about 150 kg as shown in Figure 3.2. Since vacuum potting was not used, the resin and hardener were stirred slowly to minimize bubbles in the epoxy.

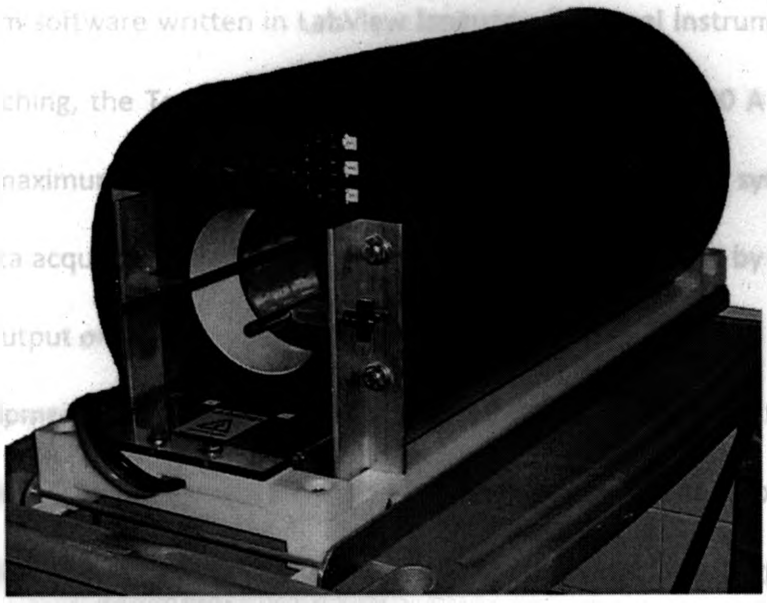

Figure 3.2. The complete insert coil. Two carbon fibre rods were used to mount the radiofrequency coil and hold the sample at the iso-center of the insert. MR compatible thermocouples allowed internal temperature measurements to be taken throughout the insert coil.

(3.2.8) Interfacing shielded B_0 coil with MRI console

Proof-of-principle imaging was performed on a (General Electric Healthcare) Sigma LX 1.5 T clinical MRI platform. The shielded B_0 insert was powered by a set of Techron 8607 amplifiers configured in a master/slave series configuration producing a maximum bipolar output of 100A. The Techron amplifiers were operated in current-regulation mode. The internal feedback circuit of the master Techron was experimentally adjusted

to match the inductance and resistance of the insert to ensure that the amplifiers faithfully reproduced the input waveforms that were generated by National Instruments data transmission/acquisition (NI DAQ) hardware and controlled by a laptop computer executing custom software written in LabView language (National Instruments, version 8.2). After matching, the Techrons could ramp the B_0 insert to ± 100 A within 5 ms, resulting in a maximum magnetic slew rate of 14 T/s. Waveform synchronization between the data acquisition device and the MRI console was achieved by means of the 'scope trigger' output of the MRI system console electronics.

The equipment room at the MRI unit housed the electronics for two separate MRI units, one clinical and one research. To limit electromagnetic noise on the control lines that regulated the Techron's output current and prevent false triggering of the current waveforms, communications between the laptop, located in the MRI control room, and the waveform generation hardware was performed via a 20 m unshielded fiberoptic Universal Serial Bus (USB) cable.

(3.2.9) Phantom for field-cycled MRI

To demonstrate the feasibility of field-cycled imaging in clinical MRI systems, a phantom was constructed that would exhibit both field-independent and field-dependent T_1 profiles. The key component was the contrast agent Vasovist (Bayer HealthCare Pharmaceuticals, gadofosveset trisodium, 0.25 mmol/mL). In its unbound form, this agent acts to shorten the T_1 of nearby water, largely independent of magnetic field

strength; however, upon binding to the protein albumin its relaxivity becomes highly field dependent. The particular choice of the Vasovist and albumin was based on the availability of the contrast agent and its well-documented relaxivity mechanisms, rather than any specific clinical or research interest in albumin.

The phantom consisted of two columns of liquid samples. The left column contained phosphate buffered saline solution (PBS) with graded concentrations of the contrast agent Vasovist. Neither the PBS nor the Vasovist demonstrated a strong dependence on magnetic field. In this column, the samples spanned a range of T_1-values; the shortest T_1-values were found in samples with the highest concentration of Vasovist. The right-hand column contained a biologically significant concentration of rabbit serum albumin (RSA) dissolved in PBS, again with varied concentrations of Vasovist. The Vasovist bound to the rabbit serum albumin creating a range of samples exhibiting varying T_1 and T_1-slope - the shortest T_1 as well as largest T_1-slope due to samples with the highest concentration of contrast agent. Therefore, the right column was expected to demonstrate a measurable change in MRI image intensity when imaged at different magnetic field strengths. See Figure 3.3.

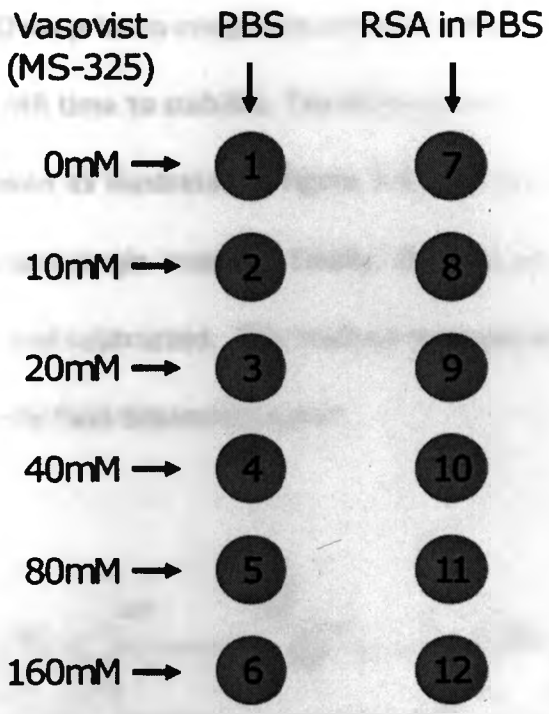

Figure 3.3. The arrangement of samples in the phantom. The left column (samples 1 to 6) contained PBS while the right column (samples 7 to 12) contained rabbit serum albumin diluted in PBS buffer at 4.5% weight/volume. Concentrations of Vasovist are given for each row, ranging from 0 to 160 μM.

(3.2.10) Pulse sequence and image acquisitions

A spin-echo pulse sequence was used to generate the MRI images, which would be used to produce the final field-cycled image. The sequence used the following parameters; 150-ms repetition time, 10-ms echo time, 31-kHz bandwidth, 8-cm field of view and a 10-mm slice thickness. The resulting scan time for each constituent image was 24 s. During the longitudinal relaxation period of each sequence, 70 mT amplitude magnetic field pulses were applied for 100-ms intervals. These ΔB pulses were completely

removed for a period of 10 ms prior to image acquisition to allow the amplifiers to settle and magnetic field of the MR time to stabilize. Ten field-increasing pulses and ten field-decreasing pulses were taken as illustrated in Figure 3.4. The ten images of each type were averaged into separate single images. Finally, the two resulting images were normalized to each other and subtracted. This method removes any field-independent signal leaving essentially only field dependent signal.

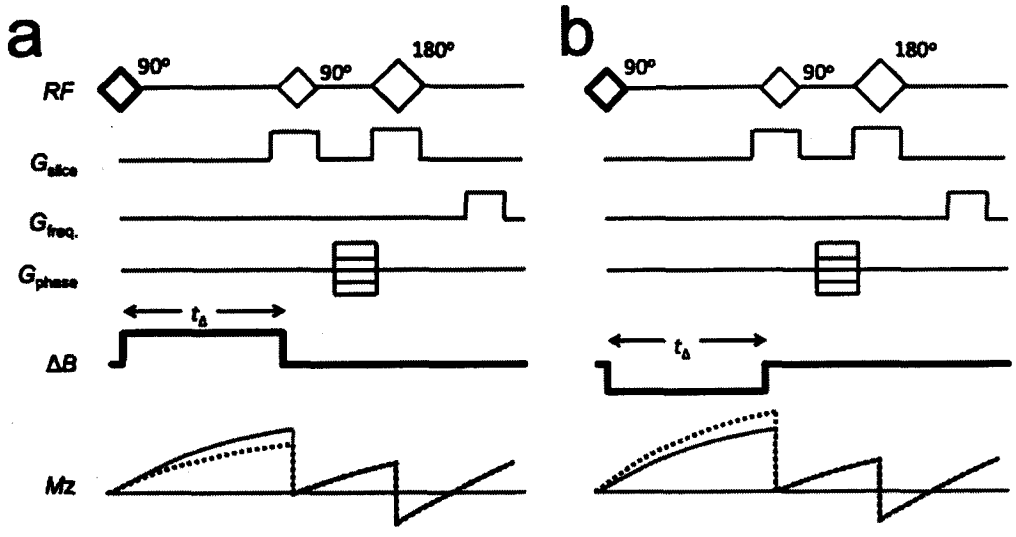

Figure 3.4. Field-cycled MRI pulse sequence. The field-increasing pulse sequence used a ΔB pulse to increase the field during the longitudinal relaxation. b) A magnetic field pulse of opposite polarity was applied during the field-decreasing pulse sequence. The amplitude and duration of the field pulses was 70 mT and 100 ms respectively. A typical spin echo pulse sequence followed approximately 10 ms after the end of the magnetic pulse.

(3.3) Results

(3.3.1) Bench Testing Insert

Inductance and resistance were measured at 12 Hz for both the primary and shield coils separately and together with an Instek 817 LCR meter (Good Will Instrument Co, Taiwan) for comparison with the design calculations. The inductance and resistance of primary and shield coils were 10 mH and 200 mΩ and 2.9 mH and 200 mΩ respectively. All measurements were taken at 20°C. The combined inductance and resistance for the assembled system (primary and shield together) were measured to be 7.0 mH and 400 mΩ, both values in excellent agreement with calculations.

The magnetic field efficiency at the isocentre of the insert coil was also measured with and without the shield with a digital Tesla meter (DTM-151, Group3 Technology, New Zealand). The efficiencies of the primary coil alone and the primary coil combined with the shield were found to be 1.0 mT/A and 0.7 mT/A respectively. As expected the counter-windings in the shield reduced the efficiency of the insert coil.

To determine the effectiveness of the shield, the net flux produced by an oscillating current was measured by placing a 1-m-diameter pickup coil around the insert. The pickup coil consisted of five turns of #20 American wire gauge magnet wire connected to a digital oscilloscope. A 100-Hz sinusoidal current was applied to the insert coil and the induced flux in the pickup coil was measured with a digital oscilloscope for configurations with and without the shield wired in series with the primary coil. Total flux through the 100-cm diameter coil concentric with the insert coil

was measured at various points along the insert's length with and without the shield. Measurements show that the addition of the shield reduced the total flux by approximately 220 times; far short of the 1400 times predicted by simulation. This discrepancy was attributed to tolerances in construction and the difference between perfect wire loops used for numerical calculation purposes versus wound solenoids.

Following the potting of the primary and shield in thermally conductive epoxy, thermal performance was evaluated by passing a direct current through the coil and monitoring thermocouple temperatures with respect to time. As well as monitoring internal temperatures the exiting water temperature was measured and the average temperature of the copper wires was determined by dynamically measuring the change in the insert's resistance as a function of time. The thermal measurements showed that for 6L/min flow of chilled water, the insert coil had a thermal resistance of 0.0175 °C/W. The greatest temperature differential was measured across the Teflon cooling lines, suggesting that relatively poor thermal conductivity of the cooling lines was the limiting factor in cooling performance.

The forces and torques experienced by the insert during regular use within the host MRI system were not quantitatively measured. However, qualitative observations suggested that the insert did not move or vibrate and no audible noise was produced.

(3.3.2) Field-Cycled Imaging

The field-increasing and field-decreasing datasets were each averaged to produce two images. These are shown in Figure 3.5a and Figure 3.5b respectively. By taking the absolute difference of these images a third image was produced in which small variations were accentuated (Figure 3.5c). The absolute different was taken to show that there were no unseen negative values in the final images. In this final image there is little to no image intensity in regions of the phantom where the relaxivity due to unbound contrast agent was largely independent of magnetic field. However, samples containing contrast agent bound to the albumin were noticeably bright since the relaxivity of activated contrast agent is highly field dependent.

While the signal to noise ratio has been measurably decreased by the subtraction process, the trade-off in image contrast cannot be understated. This method has succeeded in producing contrast that is linearly related to the concentration of Vasovist that was bound to albumin. Samples without both Vasovist and albumin bound together have been suppressed, independent of the quantity of Vasovist used.

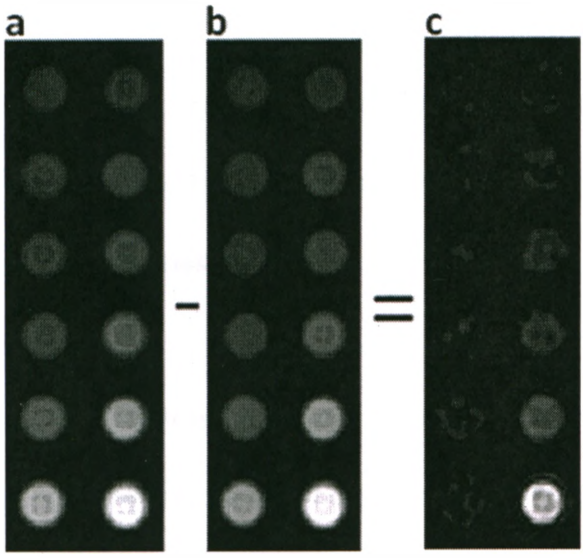

Figure 3.5. Subtraction of T_1-weighted MRI images. Images a and b show the T_1-weighted spin-echo images in which the main magnetic field was first increased and then decreased by 70 mT respectively. Image c shows the absolute difference of these images. The left column of samples, those having T_1-values which are independent of magnetic field are suppressed in intensity while in the right column samples (those with a strong magnetic field dependence) remain bright.

(3.4) Discussion

As a prototype, this insert coil has satisfactorily demonstrated that magnetic-field-dependent contrasts can be produced within a clinical, superconducting MRI magnet. Using the insert, the magnetic field was shifted by 70 mT during the imaging sequence without significant loss of MRI image quality. Improved field-cycled contrasts may be obtained by designing inserts capable of larger magnetic field shifts. This can be achieved by customizing the insert coil for each application. For example, for mouse-sized imaging our prototype should be scaled down by a factor of 2x in each dimension.

This would result in a significant increase in magnetic efficiency as well as decrease any residual coupling between insert and host system. The performance of the insert could also be increased by replacing the Teflon cooling lines with a direct cooling approach in which deionized chilled water is passed directly through the electromagnetic windings, eliminating all thermal barriers.

While improving the contrast generated by this method is important, it is the coordination of operation between the insert coil and host MRI system that remains the greatest challenge to applying this technique to a number of small-animal imaging studies. The "work around" method for pulse sequence integration described herein was tedious, requiring multiple steps just to change a single scan parameter. Currently more advanced methods of interfacing the host and the insert coil are being investigated; however, such refinements unfortunately become increasingly specific to a particular MRI platform.

(3.5) Conclusions

We have demonstrated the feasibility of design, construction, and operation of actively shielded B_0 inserts in clinical MR scanners to produce field-cycled MRI contrast. Factors including inductance, cooling, induced force, and thermal cooling must all be incorporated into the coil design. Important auxiliary details such as control of the additional hardware by the host MRI system and pulse sequence generation have been

outlined and addressed. Inductive coupling of the magnet insert with conductors contained within the MR imager has been mitigated by careful design of an active shield that has reduced this interaction by a factor of over times 200.

This work has also outlined the development of a new field-cycling-derived contrast that has the ability of differentiating between bound and unbound contrast agent. While T_1-weighted images cannot be used to distinguish unbound contrast agent from bound contrast agent, field-cycled-derived contrast images were demonstrated that exhibit image contrast related to the dependence of T_1 on magnetic field. Thus, an exciting and new approach to molecular imaging is achievable, where it is possible to remove all sources of MR image intensity which do not contain both the molecule of interest and the contrast agent which binds to it. One immediate application of this method will be to quantify the efficacy of new compounds that have been designed to bind to specific tissue proteins.

(3.6) Appendix

(3.6.1) Shield Design algorithm

Details of the shim winding depend on several physical parameters: the shield radius R_s, the maximum shield length L_s, the warm bore radius R_{wb} where the magnetic field induced by the shielded insert coil should zero and the length of the warm bore L_{wb}. In addition, there are several parameters that control the resolution of the

solution: the number of discretization points along the shield's length, *n,* and the number of target points, *m*, at the radius where shielding is desired. In some instances it is also necessary to apply a minimum current constraint to achieve a solution in which the current density in the shield is minimized. Often there can be multiple solutions, all of which produce magnetic field profiles that closely match the desired magnetic field at the target points. Designs with lower current densities naturally result in coils that have higher power efficiencies.

(3.6.2) Building the efficiency matrix

The magnetic field of the cylindrical shield is calculated from a continuous current density that is approximated by an array of *n* circular wires, or loops, of equal spacing. Unit current is assumed to flow in each of these loops. The spacing of loops is given by $\Delta x = L_s / (n - 1)$. Each circular loop is divided into a large number of straight segments or current elements for the purpose of numerical field calculation. Applying the Biot-Savart law to each current element, the total magnetic field produced at each of the *m* target locations by each loop is calculated. The *m* magnetic field values from each loop are placed into the *n*th column *m* by *n* magnetic efficiency matrix **K**. The $K_{i,j}$ value in the matrix indicates the *z*-component of the magnetic field produced by the j^{th} loop at the i^{th} target point. Figure 3.6 graphically illustrates this procedure.

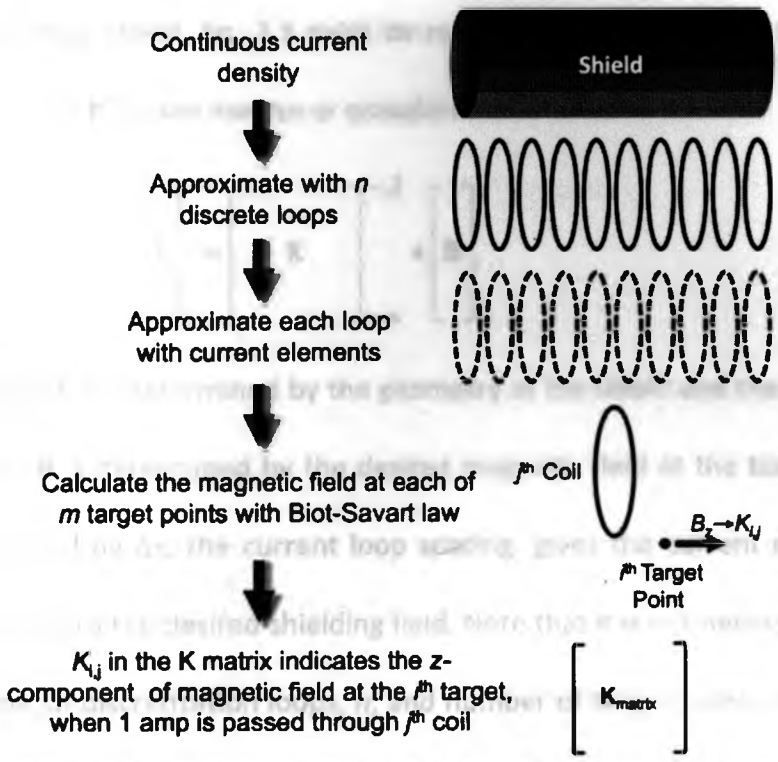

Figure 3.6. The insert design process. The design algorithm begins by breaking the shield into *n* discrete loops. Each loop is broken into short straight current elements to enable numerical calculation of the resulting magnetic field. The *z*-component of the magnetic field form the j^{th} coil at the i^{th} target point is stored in the (*i*, *j*) position of the matrix **K**.

Multiplying the matrix **K** by an *n* element current vector **I**, describing the current in each discrete loop, yields **B**, a vector of *m* elements containing the *z*-component of the magnetic field produced by the shield at the target points. Mathematically this is written as the following expression.

$$\begin{bmatrix} \mathbf{B} \end{bmatrix}_m = \begin{bmatrix} \mathbf{K} \end{bmatrix}_{m \times n} \bullet \begin{bmatrix} \mathbf{I} \end{bmatrix}_n \qquad [3.1]$$

In designing a shield, Eq. 3.1 must be rearranged to solve for **I**, the current in each loop. In Eq. 3.2 $\mathbf{K}^{-1}$ is the inverse or pseudo-inverse of **K**.

$$\left[\mathbf{I}\right]_n = \left[\mathbf{K}\right]^{-1}_{n\times m} \bullet \left[\mathbf{B}\right]_m . \qquad [3.2]$$

The matrix $\mathbf{K}^{-1}$ is determined by the geometry of the shield and the target points, while the vector **B** is determined by the desired magnetic field at the target locations. The vector **I** divided by Δx, the current loop spacing, gives the current density profile that would give rise to the desired shielding field. Note that it is not necessary to choose an equal number of discretization loops, *n*, and number of target points, *m*, so that the matrix **K** is square. For non-square matrices the pseudo-inverse of **K** can be calculated using singular value decomposition. When the matrix is over-determined the solution provided by Eq. 3.2 minimizes the functional $F = \sum_{i=1}^{m}\left(B_{i\,\text{target}} - B_{i\,\text{shield}}\right)^2$ where $B_{i\ \text{target}}$ are the *z*-components of the desired magnetic field and $B_{i\ \text{shield}}$ are the *z*-components of the magnetic field created by the shield at the i^{th} target point.

While this method produces a current density that approximates the desired field, it may not be very useful. In many situations the resulting current density will have rapidly alternating positive and negative current densities along the *z*-axis with values so large that they become impractical. To overcome this shortcoming, a minimum current constraint is added into the matrix **K** that balances the accuracy of the

magnetic field at the target points with the requirement that the current densities are zero. This constrain is incorporated by vertically concatenating the $m \times n$ matrix **K** with an $n \times n$ identity matrix that has been multiplied by a constant, ε.

$$\mathbf{K}' = \begin{bmatrix} \mathbf{K}_{1,1} & & \\ & \mathbf{K}_{1,2} & \\ & & \mathbf{K}_{m,n} \\ \varepsilon & 0 & 0 \\ 0 & \varepsilon & 0 \\ 0 & 0 & \varepsilon \end{bmatrix}_{(m+n)\times n} \qquad [3.3]$$

The solution for the currents **I** is then found from

$$\begin{bmatrix} \quad \end{bmatrix}_n = \begin{bmatrix} \quad \mathrm{K}' \quad \end{bmatrix}^{-1}_{n\times m} \bullet \begin{bmatrix} \mathrm{B} \end{bmatrix}_m . \qquad [3.4]$$

Solving this system produces a current vector **I** that minimizes the new functional F given by

$$F = \sum_{i=1}^{m} \left(B_{I\,primary} - B_{i\,shield} \right)^2 + \varepsilon \cdot \sum_{i=1}^{n} I_i^{\,2} . \qquad [3.5]$$

Here $B_{i\,\text{primary}}$ is the z-component of the magnetic field produced per unit current in the primary at the i^{th} sample point, $B_{i\,\text{shield}}$ is the magnetic field produced at the i^{th} sample point by the shield and I_i is the current in the i^{th} loop. No 'optimum' value of ε exists but rather it depends on the application and the number of discretization points, n, and the number of field constraint points, m.

(3.6.3) Creating the wire pattern

Once the current vector **I** is calculated it must be converted into a discrete wire pattern in which each wire element carries the same current. A continuous current density is approximated by interpolating the current vector along the *z*-axis and dividing the current by the loop spacing, Δx. The current density is then integrated along the positive *z*-axis recording the z-values where the integrated current density is half-integer. These axial locations represent the location of discrete wire loops approximating the theoretical current density (16). Symmetry of the magnet design yields the positions of loops along the negative *z*-axis. This is illustrated in Figure 3.7.

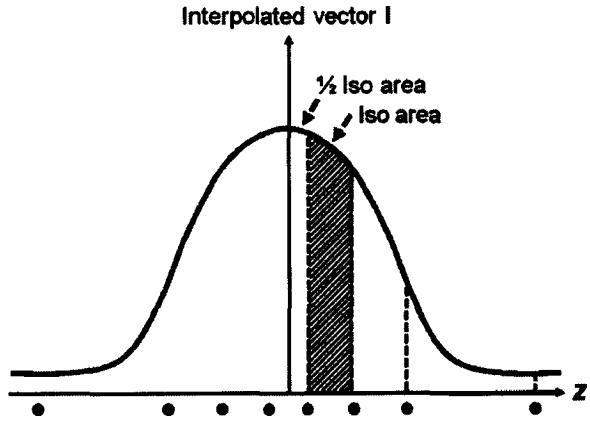

Figure 3.7. Integration of the current density. The current vector I is integrated outward from the center. Wires are placed when the area under the interpolated vector **I** equals (1/2, 3/2, 5/2, ...).

(3.7) References

1. Carlson JW, Goldhaber DM, Brito A, Kaufman L. MR relaxometry imaging. Work in progress. Radiology 1992;184(3):635-639.
2. Bottomley PA, Foster TH, Argersinger RE, Pfeifer LM. A review of normal tissue hydrogen NMR relaxation times and relaxation mechanisms from 1-100 MHz: dependence on tissue type, NMR frequency, temperature, species, excision, and age. Med Phys 1984;11(4):425-448.
3. Ungersma SE, Matter NI, Hardy JW, Venook RD, Macovski A, Conolly SM, Scott GC. Magnetic resonance imaging with T1 dispersion contrast. Magn Reson Med 2006;55(6):1362-1371.
4. Alford J. From static to dynamic: Construction of an actively shielded B_0 coil for field-cycled imaging with clinical MR platforms. ISMRM. Toronto, Canada; 2008.
5. Gilbert KM, Handler WB, Scholl TJ, Odegaard JW, Chronik BA. Design of field-cycled magnetic resonance systems for small animal imaging. Phys Med Biol 2006;51(11):2825-2841.
6. Lurie DJ, Foster MA, Yeung D, Hutchison JM. Design, construction and use of a large-sample field-cycled PEDRI imager. Phys Med Biol 1998;43(7):1877-1886.
7. Alford JK. Delta Relaxation Enhanced MR: Improving activation-specificity of molecular probes through R1 dispersion imaging. Magnetic Res in Medicine 2008;In Press.
8. Alford JK. Delta relaxation enhanced MR (dreMR): Theory of T1-slope weighted contrast. ISMRM. Toronto, Canada; 2008.
9. Eldredge HB, Spiller M, Chasse JM, Greenwood MT, Caravan P. Species dependence on plasma protein binding and relaxivity of the gadolinium-based MRI contrast agent MS-325. Investigative radiology 2006;41(3):229-243.
10. Overoye-Chan K, Koerner S, Looby RJ, Kolodziej AF, Zech SG, Deng Q, Chasse JM, McMurry TJ, Caravan P. EP-2104R: a fibrin-specific gadolinium-Based MRI contrast agent for detection of thrombus. Journal of the American Chemical Society 2008;130(18):6025-6039.
11. Zhou X, Caravan P, Clarkson RB, Westlund PO. On the philosophy of optimizing contrast agents. An analysis of 1H NMRD profiles and ESR lineshapes of the Gd(III)complex MS-325+HSA. J Magn Reson 2004;167(1):147-160.
12. Matter NI, Scott GC, Grafendorfer T, Macovski A, Conolly SM. Rapid polarizing field cycling in magnetic resonance imaging. IEEE Trans Med Imaging 2006;25(1):84-93.
13. Montgomery DB. Solenoid Magnet Design: Wiley-Interscience; 1969.
14. Siakavellas NJ. Two simple models for analytical calculation of eddy currents in thin conducting plates. Magnetics, IEEE Transactions on 1997;33(3):2245-2257.

15. Mansfield P, Chapman B. Active magnetic screening of coils for static and time-dependent magnetic field generation in NMR imaging. Journal of Physics E: Scientific Instruments 1986(7):540.
16. Bowtell R, Mansfield P. Gradient coil design using active magnetic screening. Magn Reson Med 1991;17(1):15-19; discussion 19-21.

Chapter 4 – Improving the dreMR system

(4.1) Introduction

Chapters Two and Three of this thesis introduced delta relaxation enhanced MR (dreMR) (1,2), a method for performing molecular imaging, which utilizes an insertable electromagnetic coil to manipulate the strength of the main magnetic field during the imaging pulse sequence. The prototype dreMR coil described in those chapters demonstrated the concept of dreMR; however, certain design flaws quickly became evident. The insert coil was too small to be used for human, or large-animal, imaging and too large to produce the ½-Tesla, or better, magnetic field shifts desired for mouse imaging. Factors limiting the field shift included; the magnetic efficiency of the coil, the rate that heat was deposited into the coil (i.e. electrical resistance) and the rate at which heat was removed from the coil. A second flaw was its significant weight. To ensure that the coil did not move or vibrate during imaging, it had been purposefully engineered to be quite massive. Upon completion, it was realized that the coil was too massive to be readily inserted and removed from the host MRI system without significant difficulty. The third, and perhaps most significant, problem was in fact current instability in the gradient amplifiers that powered the insert coil. This instability produced image distortions and artefacts such as increased noise, blurring and image shifting.

(4.2) Methods Part 1 – System Improvements

Each of the aforementioned limitations was addressed in the design and construction of a second generation dreMR coil. Reducing the physical size of the insert coil decreased its mass, increased its magnetic efficiency and lowered its inductance and electrical resistance. System cooling was significantly improved by channeling the coolant directly through the magnet windings rather than through Teflon tubing, a method used in the earlier design. To eliminate the current instability issuing from the gradient amplifiers, a high-speed, solid-state switch box was inserted between the amplifier and the insert coil to electrically isolate (disconnect) the amplifiers from the electromagnetic insert during data acquisition.

(4.2.1) Decreasing the Size and Mass of the Insert Coil

The inner diameter of the coil was reduced from 17 to 8 cm, the outer-diameter decreased from 41 to 32 cm and the length decreased from 76 to 42 cm. The 8-cm inner diameter was sufficient to contain a RF coil, RF shield and small rodent.

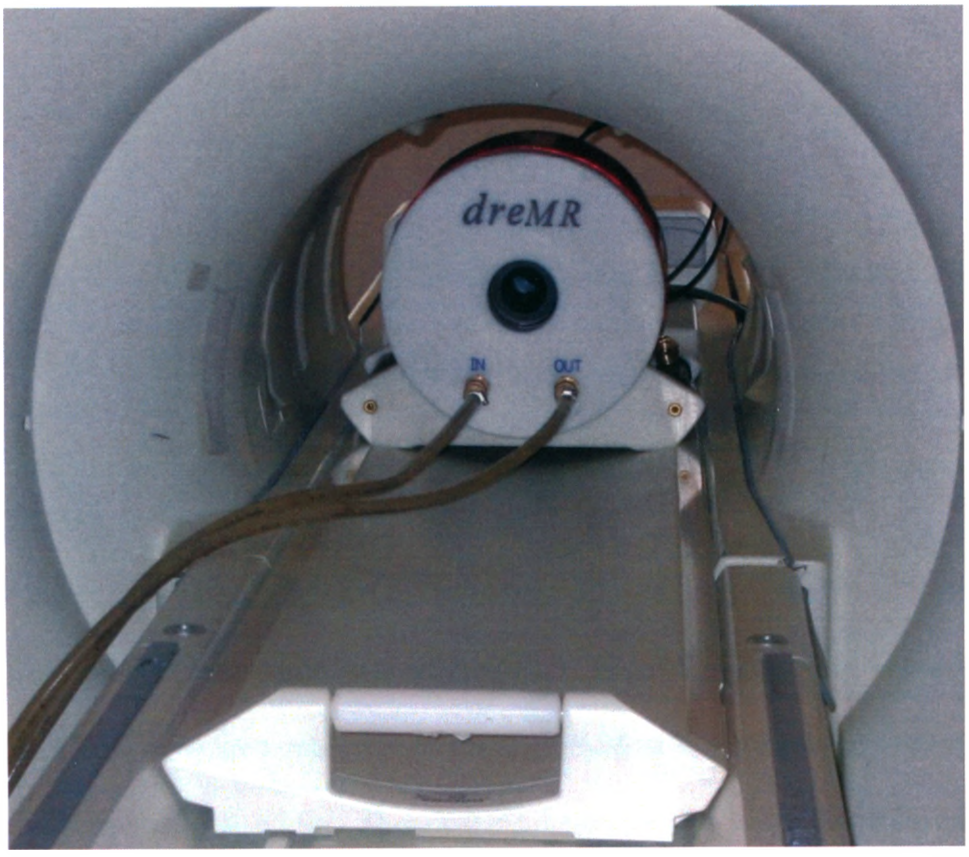

Figure 4.1. The dreMR electromagnetic insert rests upon the patient bed of an MRI machine. In this image, the cooling lines are visible.

(4.2.2) Increasing Coil Performance

Magnetic efficiency and electrical resistance are two important factors in determining the maximum continuous magnetic field shift that may be produced by an insert coil. Efficiency of an electromagnet is expressed in terms of the magnitude of the magnetic field shift per ampere of current flow. The resistive merit is a measure of the magnitude of magnetic field that can be produced for a given rate of heat deposition. The resistive merit is the coil efficiency, η, divided by the square root of the coil resistance.

$$merit_R = \eta/\sqrt{R} \qquad [4.1]$$

Changing the electromagnetic coil's geometry can have significant impact on efficiency and, resistance and resistive merit.

(4.2.3) Improving dreMR Coil Cooling

The rate of heat transfer from the coil was increased by substituting hollow copper wire (Small Tube Products, Duncansville, USA) for the #5 AWG magnet wire used in the prototype. The hollow wire was custom-made with a 5 mm, square outer diameter and a 3 mm, circular inner diameter. Electrical insulation for the wire was achieved with a continuously wound, double layer of 0.125 mm Kapton. While the substitution of hollow wire increased the electrical resistance of the coil by 30%, it provided a vastly superior cooling mechanism by permitting chilled water to flow directly through the hot electrical conductor. This method provides intimate contact between the coolant and the copper windings, enhancing cooling efficiency. Efficient heat removal lowers the operating temperature of the insert coil and allows it to operate at higher currents. The water fittings for the electrical conductors are shown in Figure 4.2.

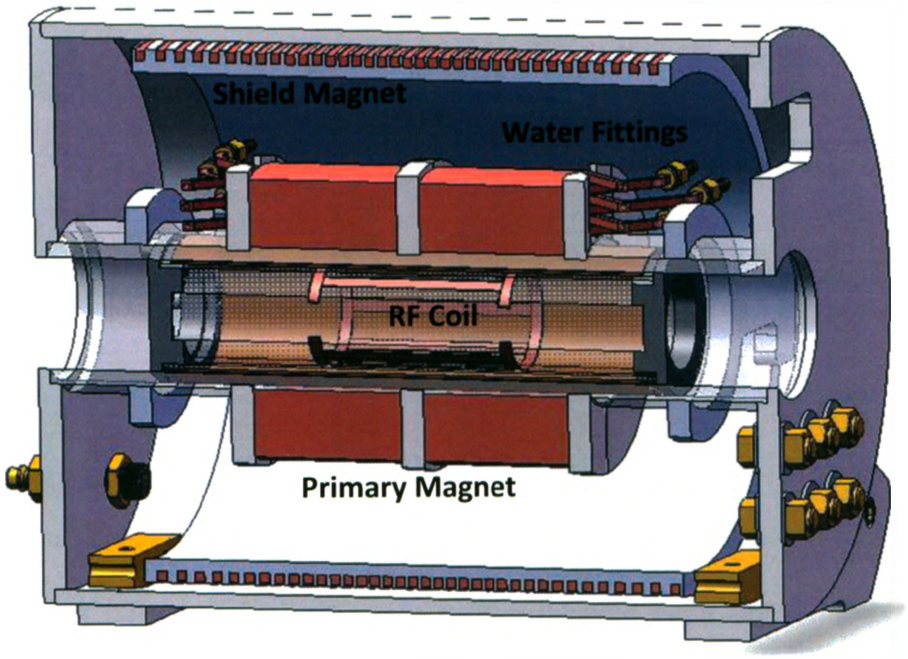

Figure 4.2. A computer drafted drawing of the 2nd generation dreMR system. The manifold is not shown.

Functionally, a shielded solenoid coil has a primary magnet for producing the field shift and a shield magnet for limiting magnetic interactions between the solenoid and the host MRI system. For ease of construction and to achieve a fourfold increase in cooling, both the primary and the shield magnets were constructed in two parts. Through the use of a Teflon manifold system, the cooling water was routed through the coil in eight parallel paths, while the electrical current passed through each conductor in series. See Figure 4.3.

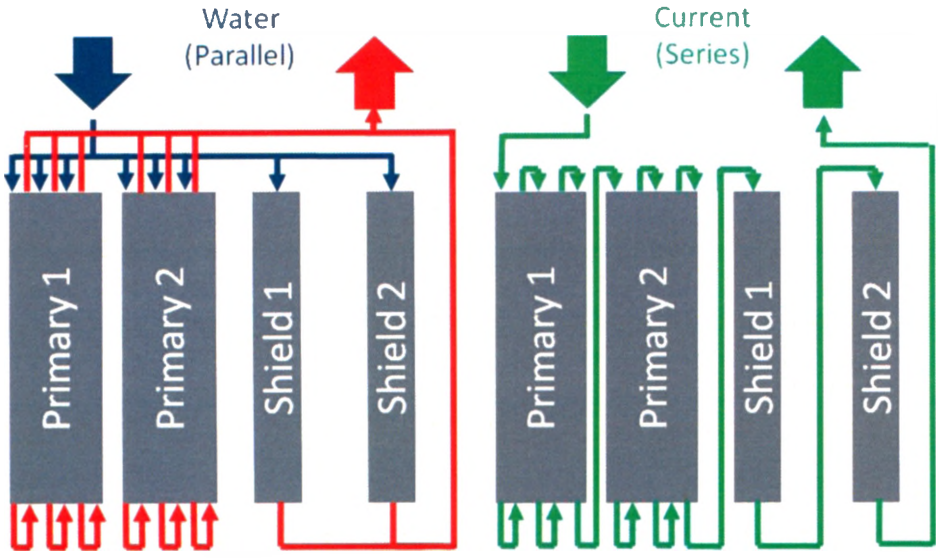

Figure 4.3. The chilled water was routed through eight parallel paths. Each of the primary halves has three flow paths while each of the shield halves has one. Electrically, the insert electromagnet was wired in series, with the same current flowing through every part of the device.

(4.2.4) Current Instability

The 2nd generation dreMR coil had a significantly higher efficiency than the first coil (0.85 mT/A), translating each ampere of input current into a 36 kHz shift in the Larmor frequency. The magnetic efficiency of a dreMR coil can be several orders of magnitude stronger than that of a high-performance full body gradient coil. So, even relatively small electrical instabilities in the dreMR coil current would be directly and efficiently translated into magnetic field instability. For example, a one milli-amp of current instability in the 2nd-generation dreMR coil would result in a 6ppm of inhomogeneity across a 5-cm sample and a 350 Hz frequency shift. If the instability changed during image acquisition, it would result in artefacts in the final image. To prevent instabilities

from entering the dreMR coil during image acquisition a high-speed, high-current switch box was placed between the power supply and the insert coil to electrically isolate one input lead of the dreMR insert coil from the power supply. In this application, the power supply system consists of one or more gradient amplifiers used in current-control (or constant current) mode. In current-control mode, the output voltage of the amplifiers will self-adjust to maintain the desired current.

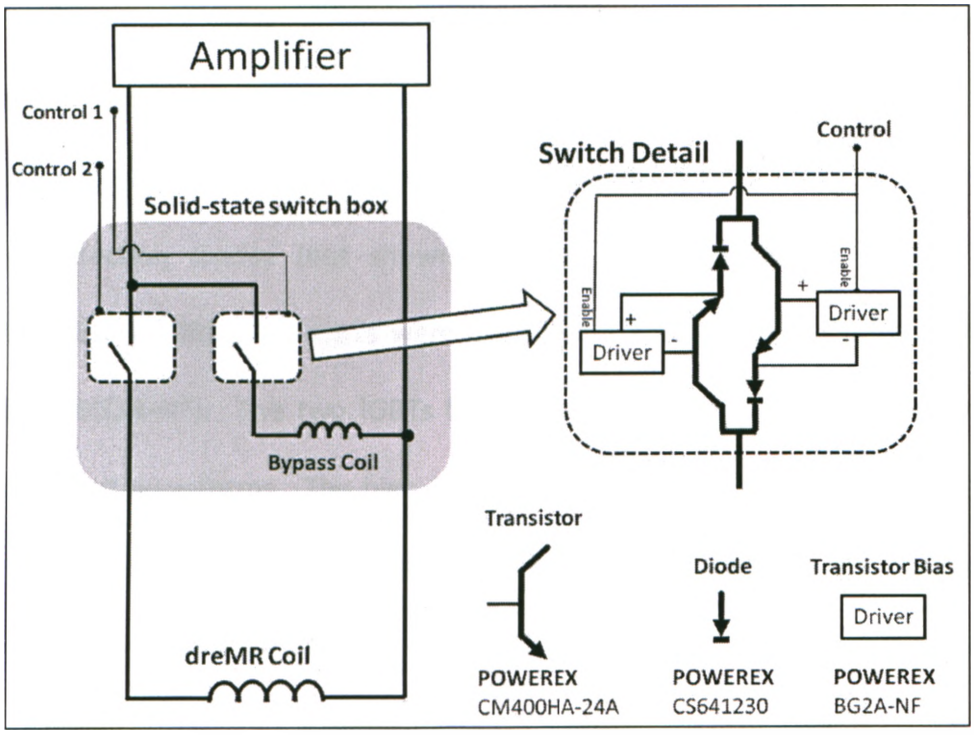

Figure 4.4. A switch box was used in order to electrically disconnect the dreMR insert coil from the amplifier during image acquisition. The switch box removes any offset currents or noise during image acquisition.

(4.2.5) Isolating the dreMR Insert Magnet

Because current-controlled amplifiers are designed to have an inductive load be present at all times, when the dreMR coil is isolated from the amplifier an auxiliary (bypass) load must be substituted. Our auxiliary load was a small electromagnetic solenoid, physically located within the switch box. Individual control of each current path permitted the switch box to be operated on a "make before break" rule so that at least one coil was attached to the power supply at any given time. A circuit diagram with the amplifier, dreMR coil and solid-state switch box is shown in Figure 4.4. The switch box circuit contained two custom-built, solid-state sub-switches. Each sub-switch was built with two, 400 A, 1200 V, insulted gate bipolar transistors (IGBT) (POWEREX 400HA-24A) with built-in protection diodes (not shown in figure) and two 300 A, 1200 V diodes (POWEREX CS641230). The IGBTs were biased with an optically-isolated driver circuit (POWEREX BG2A-NF). The two IGBTs for each current path were necessary to allow bipolar current waveforms. The high-current diodes were required to prevent reverse current from shunting through the transistors' protection diode while the transistor was in the off (non-conducting) state.

(4.2.6) Performance of the Switch Box

Based on product literature, the maximum continuous current for the switchbox was 300 A (limited by the diode), and the maximum peak current was 800 A (limited by the IGBT). To prevent overheating of the switch box components, the circuit was mounted

on a 19-inch wide, 1000 W heat sink (TW7-1275-flsx, D6 Industries, Massachusetts, USA).

The same literature claimed a 800 ns switching time for the diode and a 600 ns time for the IGBT. Given that only a 1 ms switching time was required for this application, both components operated much faster than required.

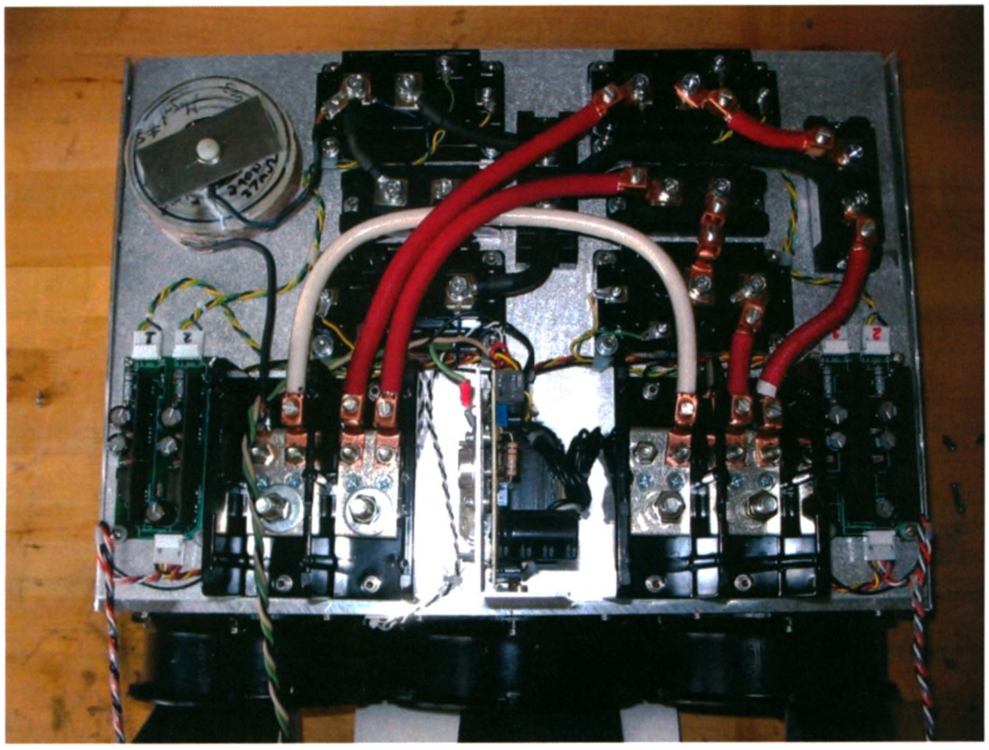

Figure 4.5. The high-current solid-state switch box was built on a 1000 W heat sink with three cooling fans. The heat sink was designed for mounting in a standard 19-inch rack. The bypass solenoid was positioned at the top left-hand side of the heat sink.

(4.3) Methods Part 2 - System Performance

Two experiments were performed with the 2nd-generation dreMR system. The first experiment demonstrated the ability of the disconnect switch to remove electrical instabilities during image acquisition. Because the disconnection circuit used solid-state transistors to open and close the connection and did not physically separate the dreMR coil from the amplifiers, it was necessary to verify that sufficient electrical isolation was obtained. The second experiment was performed to verify that the dreMR coil could produce powerful magnetic field pulses during the relaxation portion of an MRI pulse sequence without seriously degrading image quality.

(4.3.1) Phantom and RF Coil

For both experiments, the same phantom and RF coil were utilized. The phantom consisted of a rectangular matrix of fifteen nuclear magnetic resonance (NMR) sample tubes arranged into three columns of five rows. The tubes had an inner diameter of 4 mm and were cut to a length of 25 mm. To prevent an air/water susceptibility artefact, the tubes were inserted into a high-density polyethylene holder. The tubes contained samples of deionized water with various levels of rabbit serum albumin and/or the albumin-binding contrast agent MS-325 (3-5). In the presence of albumin, MS-325 displays a highly magnetic field dependent relaxivity, while in the absence of albumin the agent displays no measurable magnetic field dependence (see Figure 1.4 in Chapter

1). The left column of the phantom contained increasing levels of MS-325 but no albumin. See

Figure 4.6 for the MS-325 concentration levels. For these samples, one should expect to see the relaxation rates of this column increase with MS-325 concentration, but no magnetic field dependence of relaxation rates at any concentration level. The middle column contained only water and acted as a control. Again, one should not expect to see measurable magnetic field dependence in these samples. The right column contained rabbit albumin at a 600 μM concentration and the same MS-325 concentration levels as the left column. One should expect to see R_1 increase with MS-325 concentration and, more importantly, also see a strong R_1 dependence on magnetic field strength for all samples.

The RF coil was a custom built, eight rung, high-pass, birdcage coil tuned for 1.5 T (Figure 4.2). To reduce noise and coupling between the RF coil and the dreMR insert coil a cylindrical RF shield was used.

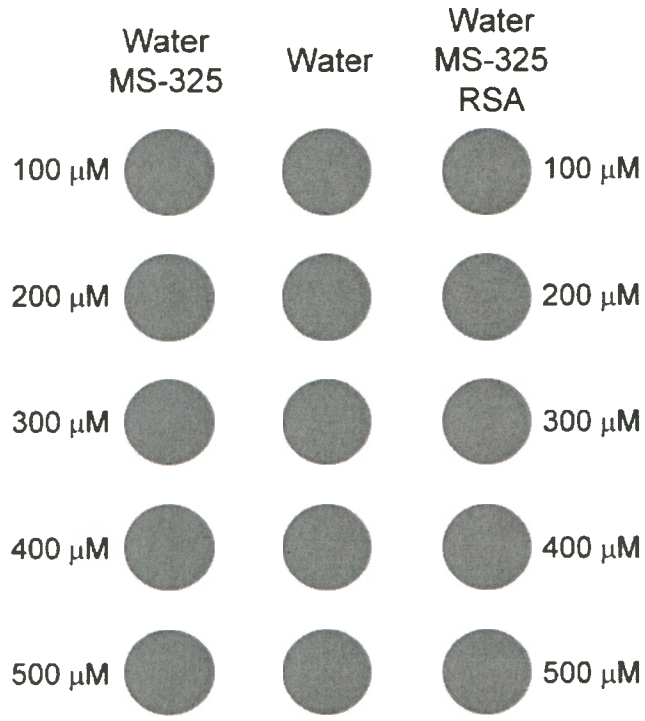

Figure 4.6. The phantom consisted of three columns of samples. The first column (left) was deionized water with MS-325 (Vasovist) in concentrations of 100, 200, 300, 400 and 500 μM. The second column contained only deionized water. The third column (right) contained a rabbit serum albumin (RSA) and water mixture 600 μM concentration and MS-325 in identical concentrations to the first column.

(4.3.2) Evaluating the Solid-State-Switch

To evaluate the effectiveness of the switch box; the insert coil, with RF coil and phantom, was placed inside a 1.5 T GE Sigma LX MR system (GE Healthcare) and electrically connected (via the switch box) to a set of *AE*Techron 7796 amplifiers (*AE*Techron, Indiana, USA) configured in a parallel, master/slave arrangement. The master and slave amplifiers were matched to one another by adjusting their output

gains and offsets to minimize electrical instabilities in the output current. The feedback compensation circuit of the master amplifier was experimentally matched to the dreMR insert coil.

MR images (see Figure 4.7) were acquired with a spoiled gradient recalled echo sequence using the following sequence parameters: TR = 100 ms, TE = 6.4 ms, slice thickness = 4 mm, voxel size 0.32 x 0.32 mm, bandwidth = 122 Hz/pixel, field-of-view = 8 cm, flip angle = 30°, matrix size = 192 x 192, num. averages = 1. The 192 x 192 matrix was interpolated to a 256 x 256 image after acquisition. No dreMR pulse was applied during the acquisition of either image. The first MR image was acquired with the switch box in the 'open' configuration such that the dreMR coil was electrically isolated from the power supplies during image acquisition. The second image was acquired with the solid-state switch in the 'closed' configuration. In this state the dreMR insert coil was electrically connected to the amplifiers during image acquisition but held at zero current.

(4.3.3) Evaluating the dreMR Coil

To evaluate the ability of the dreMR coil to produce a powerful magnetic field shift during an MRI pulse sequence, two MRI images were acquired (Figure 4.8). The first image was a regular (non-dreMR) spoiled gradient recalled echo (SPGR) sequence. For the second image, a 175 A, 150 mT magnetic field (ΔB) pulse was applied during the relaxation portion of the sequence. The following parameters were used for both

images: TR = 100 ms, TE = 5.1 ms, slice thickness = 2 mm, voxel size 0.32 x 0.32 mm, bandwidth = 244 Hz/pixel, field-of-view = 8 cm, flip angle = 30°, matrix size = 192 x 192, num. averages = 1. The 192 x 192 matrix was interpolated to a 256 x 256 image following acquisition. For the second image, in which a ΔB pulse was applied during the relaxation portion of the pulse sequence, the ramp time of the ΔB pulse was 5 ms. The dreMR pulses were initiated at the start of the relaxation portion of the pulse sequence and completed 1-ms before the RF pulse of the following acquisition. All shimming and setup parameters were determined before application of the dreMR pulse. When acquiring the second image, no changes to shimming or RF center frequency were made.

(4.4) Results

(4.4.1) Design Summary for 2nd-Generation dreMR Electromagnet

Table 4.1 compares several key parameters of the two dreMR systems, including mass, physical dimensions, and electrical properties.

	Prototype dreMR Coil	2nd-gen. dreMR Coil	Units
Mass	150	50	[kg]
Length	76	42	[cm]
Inner Diameter	17	8	[cm]
Outer Diameter	41	32	[cm]
Inductance	7	1.2	[mH]
DC Resistance	400	120	[mΩ]
Imaging Region	14	5	[cm]
Mag. Efficiency	0.7	0.85	[mT / A]
Resistive Merit	1.1	2.5	[mT A^{-1} $\Omega^{-1/2}$]
Max. Cont. Field	70 (70 °C rise)	270 (30 °C rise)	[mT]

Table 4.1. Direct comparison of the prototype and 2nd-generation dreMR electromagnetic insert coils.

(4.4.2) Efficiency and Merit

The prototype dreMR system had an efficiency of 0.7 mT/A, while the 2nd generation system had an improved efficiency of 0.85 mT/A. The resistive merits of the prototype and 2nd generation dreMR coils were 1.1 and 2.5 mT A^{-1} $\Omega^{-1/2}$ respectively, an increase of 2.3 times. This indicates that for a given rate of heat deposition, the 2nd generation coil could produce a magnetic field shift 2.3 times larger than the prototype coil. For example, the maximum sustained power dissipation for the prototype coil was 4 kW, corresponding to a continuous 70 mT field shift. For the same 4 kW input power, the 2nd-generation coil can achieve the 2.3 times larger shift of 160 mT.

(4.4.3) Insert Cooling

At 300 kPa of water pressure, the measured flow through the insert coil was 100 mL/s. A 30 °C temperature rise in the cooling water would correspond to 12.3 kW of heat

dissipated and a sustained field shift of 270 mT. In comparison, at the same flow rate the prototype dreMR coil experienced an internal temperature rise of 70°C while generating only a 70-mT field shift. Due to poor heat conduction between the electrical wire and the cooling channels of the insert coil, only 4 kW of heat was dissipated at this temperature.

(4.4.4) Solid-State Switch Performance

The MR image in which the dreMR coil was electrically isolated (switch open) from the amplifiers during image acquisition is shown in Figure 4.7-left. This image appeared to be artefact free. The MRI image in which the dreMR coil was electrically connected (switch closed) to the amplifiers during image acquisition is shown in Figure 4.7-right. In this image, significant ghosting appeared both in the phase encoding direction (horizontal) while minor blurring appeared in the frequency encoding direction (vertical).

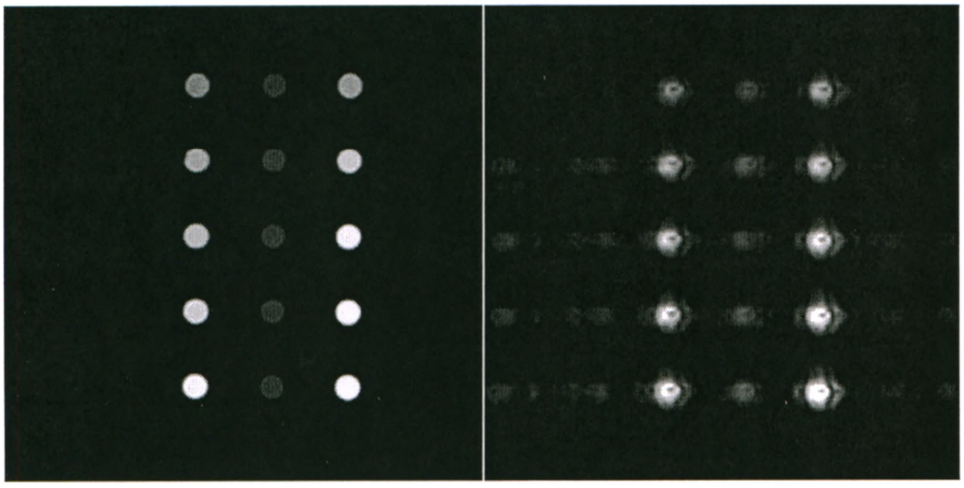

Figure 4.7. For both images, the dreMR insert coil was attached to the amplifiers and the amplifiers were enabled. No current waveforms were applied to the insert for either image; this test was to demonstrate the effect of background instability in the amplifiers. For the image on the left, one input lead of the dreMR coil was electrically isolated from the insert by "opening" the disconnect switch. For the image on the right, the insert coil was not isolated. Obviously, there is a significant amount of image distortion and ghosting without electrical isolation.

(4.4.5) Insert Coil Performance

The regular SPGR image (Figure 4.8-left) and the dreMR-SPGR image (Figure 4.8-right) both appeared to be free of ghosting and blurring. The 150 mT dreMR pulse resulted in a 10% increase in the steady state magnetization of all samples. In order to normalize the steady-state magnetization of the non-dreMR and dreMR images, it was necessary to reduce the magnitude of the dreMR image 10%. Following normalization the second image was subtracted from the first image. The result of this subtraction is shown in Figure 4.8 (bottom). The relative noise in the subtracted image is significantly higher

than in the constituent images; however, specificity to the presence of the albumin was obviously obtained.

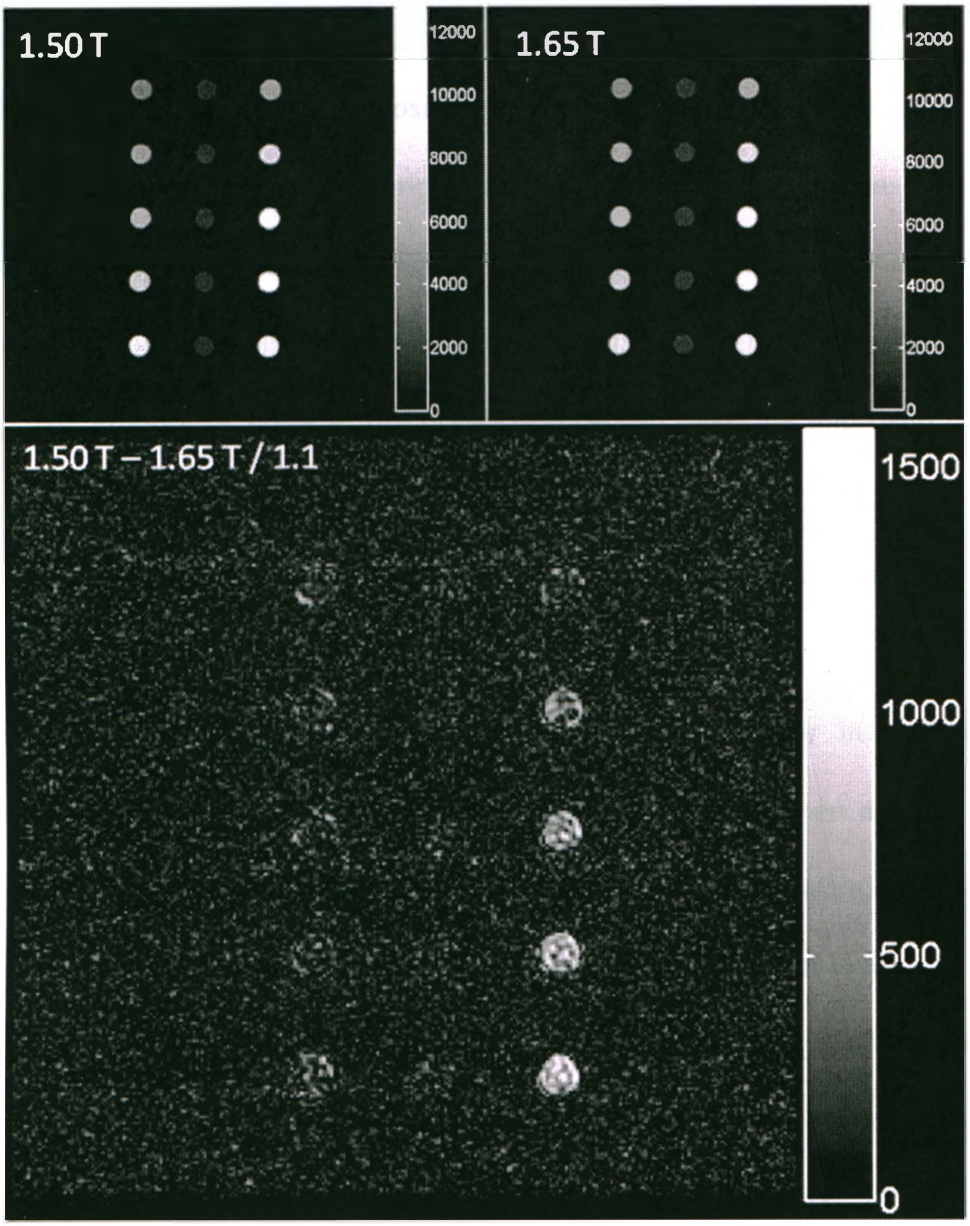

Figure 4.8. Top left: Spoiled gradient recalled echo (SPGR) sequence image. Top right: The same sequence was used, but the relaxation magnetic field strength has been increased from 1.5 T to 1.65 T during the relaxation portion of the pulse sequence. Bottom: Magnetic field dependence of the sample is obtained by subtracting the second image from the first following normalization.

(4.5) Discussion

Figure 4.8-bottom shows that it is possible to produce image contrast related to the magnetic field dependence of the sample. Only contrast from the samples containing the magnetic field dependent albumin-MS-325 complex remained after subtraction. Other samples, which contained water or water with MS-325, were suppressed from the image. The amount of noise in the dreMR-subtraction might be improved through several methods including: better RF coil(s), parallel imaging, optimized pulse sequences, increased number of averages or lowering of the acquisition bandwidth. Regarding the final item on the list; it was found that when the bandwidth was significantly lowered image blurring and distortion would appear in dreMR-SPGR sequences. Figure 4.9 shows blurring in the readout direction when a much lower bandwidth of 72Hz/pixel was used. The other sequence parameters were: TR = 100 ms, TE = 8 ms, slice thickness = 4 mm, voxel size 0.32 x 0.32 mm, field-of-view = 8 cm, flip angle = 30°, matrix size = 192 x 192, num. averages = 1. The 192 x 192 matrix was interpolated by to a 256 x 256 image following acquisition. The amplitude of the applied dreMR pulse was 100 mT. In all sequences, the TE was automatically minimized by the MR console. The images in Figure 4.8 were acquired with a TE of 5.1 ms, while the image in Figure 4.9 was acquired with a TE of 8.0 ms. Since the dreMR coil was electrically isolated from the amplifiers during image acquisition, this blurring and distortion is likely due to a time-dependent, repeatable source of instability in the magnetic field, unrelated to the amplifiers. We hypothesize that this instability is due to

eddy currents induced in the MRI system during field-shifting through inductive coupling between the host MRI and the dreMR insert.

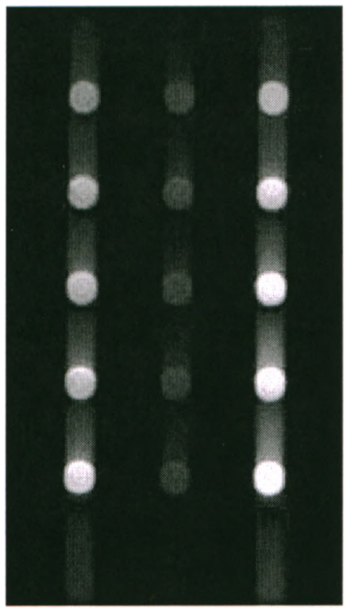

Figure 4.9. Blurring in the frequency encoding direction appears when the bandwidth is lowered. This may be due to eddy currents generated in the superconducting MRI by dreMR coil.

(4.6) Conclusions

The 2nd-generation dreMR coil is a unique tool for investigating the magnetic field dependence of sample relaxation rates. Magnetic field shifts of 150 mT were achieved within a clinical 1.5 T system without significant reduction in image quality. The ability to produce unique contrast, related to the magnetic field dependence of the pulse sequence, was demonstrated. The 2nd-generation dreMR system described here is

smaller, lighter and more powerful than the previous dreMR coil and as such is much closer to a general usage, commercially available research tool.

(4.7) References

1. Alford JK. Delta relaxation enhanced MR (dreMR): Theory of T1-slope weighted contrast. ISMRM. Toronto, Canada; 2008.
2. Alford JK. Delta Relaxation Enhanced MR: Improving activation-specificity of molecular probes through R1 dispersion imaging. Magnetic Res in Medicine 2008;In Press.
3. Caravan P, Cloutier NJ, Greenfield MT, McDermid SA, Dunham SU, Bulte JW, Amedio JC, Jr., Looby RJ, Supkowski RM, Horrocks WD, Jr., McMurry TJ, Lauffer RB. The interaction of MS-325 with human serum albumin and its effect on proton relaxation rates. Journal of the American Chemical Society 2002;124(12):3152-3162.
4. Rohrer M, Bauer H, Mintorovitch J, Requardt M, Weinmann HJ. Comparison of magnetic properties of MRI contrast media solutions at different magnetic field strengths. Investigative radiology 2005;40(11):715-724.
5. Eldredge HB, Spiller M, Chasse JM, Greenwood MT, Caravan P. Species dependence on plasma protein binding and relaxivity of the gadolinium-based MRI contrast agent MS-325. Investigative radiology 2006;41(3):229-243.

Chapter 5 – The dreMR double inversion recovery pulse sequence

(5.1) Introduction

The recent development of delta relaxation enhanced MR (dreMR) (1) has provided a unique method for determining the binding (activation) state of targeted, T_1-shortening MRI contrast agents (2-5). In Chapters 2, 3 and 4 magnetic field dependence in R_1 was determined by the subtraction of two images, which were acquired at different magnetic field strengths. In this Chapter, a single-shot sequence is investigated for developing dreMR contrast.

Though the dreMR subtraction sequences are easily understood and adequately demonstrate the ability to produce magnetic field dependent contrast, they are extremely sensitive to magnetic field instabilities. Ideally, in all dreMR sequences the main magnetic field should be returned to its static strength prior to image acquisition. However, it has been found that small field shifts persist during image acquisition. An image-to-image variation of as little as 3 μT (127 Hz) in the main magnetic field strength during acquisition can result in noticeable image shifting in the readout direction. Even a single voxel shift in the constituent images can result in significant artefact following image subtraction. Though animal imaging has not yet been attempted, it is expected that any movement will produce additional subtraction artefacts.

Herein, a single-shot double inversion recovery (DIR) dreMR pulse sequence is described for acquiring dreMR images within a single acquisition. The advantage of the single-shot approach is that it does not require subtraction or other post-processing to produce image intensity related to the magnetic field dependence of the longitudinal relaxation rate (R_1) of the sample. Similar to how inversion recovery sequences are used to suppress or "null" signal from specific tissue types, the dreMR-DIR sequence nulls MR signal from all tissues without magnetic field dependent relaxation rates. In addition, like standard inversion recovery sequences, the inversion timing of the dreMR-DIR sequence is application specific. For dreMR-DIR the inversion timing is determined by the anticipated range of relaxation rate (R_1) values within the sample. In the following Theory section, the evolution of magnetization for both magnetic field dependent and magnetic field independent samples was simulated during a dreMR-DIR sequence by numerically solving the differential Bloch equations of magnetization. This computer simulation used idealized tissue models and should only be thought of as an instructional aid to help in understanding the DIR sequence. In the Methods section, the simulation was used to investigate whether significant dreMR style contrast could be achieved with the DIR sequence for a common collection of biological tissues and an albumin-binding targeted contrast agent.

(5.2) Theory

With delta relaxation enhanced MR it becomes possible to translate the dependence of R_1 on magnetic field strength ($\partial R_1/\partial B$) into measurable magnetization by changing the main magnetic field strength of the MRI system during the pulse sequence. However, this ability does not automatically prevent other, more familiar, sources of contrast from appearing in the final image. Therefore, maximization of contrast derived from $\partial R_1/\partial B$ while suppressing contrast for field independent sources requires highly specific pulse sequences. For simplicity and brevity, the dependence of relaxation rate upon magnetic field strength, $\partial R_1/\partial B$ will hereafter be abbreviated to R_1'.

The magnetization at some position (*x, y, z*) within the sample will depend on the local density of magnetic moments, their relaxation rates, and parameters of the applied pulse sequence (as well as other effects that we will ignore, such as diffusion). Let us express the magnetization at the end of the relaxation period of the pulse sequence as the sum of two functions *A(...)* and *B(...)*. The function *A(...)* will contain the magnetic field dependence upon R_1, while the function *B(...)* will account for all magnetization due to R_1'. In traditional MRI, there is no magnetization from R_1' and therefore *B(...)* = 0 and $M(x,y,z) = A\left(other\ seq.\ params., R_1\right)$. When the ability to change the magnetic field during a pulse sequence is added, the final magnetization is written as:

$$M(x,y,z) = A\left(other\ seq.\ params., R_1\right) + B\left(other\ seq.\ params., \Delta B, R_1'\right) \quad [5.1]$$

The ideal dreMR sequence would maximize *B(...)*, reduce *A(...)* to zero, and produce magnetization that is as linear as possible to R_1'. The linear requirement is added so that relative measurements of bound contrast agent concentrations can be made from image intensity. Combining all three requirements results in Eq. 5.2.

$$M(x,y,z) = B\left(other\ seq.\ params.\right) \cdot \Delta B \cdot R_1' \quad [5.2]$$

A consequence of Eq. 5.2 is that when $R_1' = 0\ s^{-1}T^{-1}$, the magnetization, *M(x, y, z)*, is also zero at the moment of measurement. Since dreMR assumes that R_1' arises from magnetic field dependence in longitudinal relaxivity (i.e. $R_1' \propto \partial r_1/\partial B$), Eq. 5.2 may be modified accordingly.

$$M(x,y,z) = B\left(other\ seq.\ params.\right) \cdot \Delta B \cdot \partial r_1/\partial B \quad [5.3]$$

Because only bound contrast agent shows any significant $\partial r_1/\partial B$, magnetization is prepared that is specific to the binding state of the targeted contrast agent binding.

(5.2.1) The Double Inversion Sequence

The double inversion recovery (DIR) dreMR sequence is one method for directly (i.e. without post processing) preparing sample magnetization based upon R_1'. During the relaxation portion of the sequence, two ΔB pulses and two RF inversion pulses are applied in such a manner as to maximize the dependence on R_1' and minimize dependence on R_1 at the completion of the relaxation part of the sequence (start of image acquisition). This approach is more sophisticated but similar to standard inversion recovery sequences where the inversion time is chosen to reduce magnetization from fat or water. An example DIR dreMR sequence is shown in Figure 5.1, where ΔB pulses of 200 mT are used to first increase and then decrease a static 3 T magnetic field. The DIR dreMR sequence has three components: the correction period, the positive ΔB period and the negative ΔB period. During the correction period, magnetization is allowed to evolve at the static field strength, whereas during the positive and negative ΔB periods the magnetization evolves first at 3.2 T and then at 2.8 T.

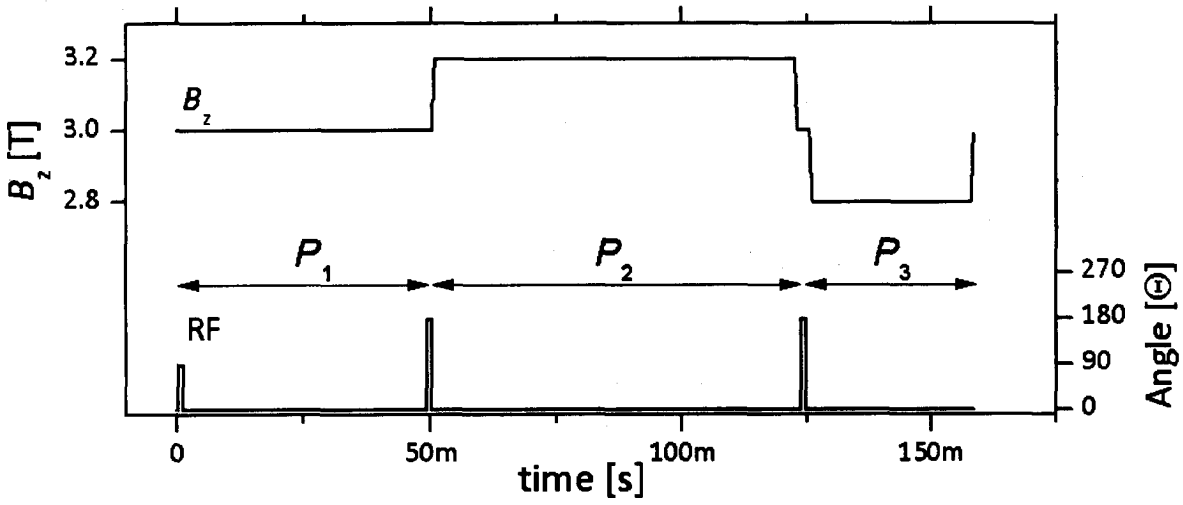

Figure 5.1. The double inversion dreMR pulse produces magnetization based upon the magnetic field dependence of R_1 by the application of a series of magnetic field shifts and RF inversion pulses. The image acquisition portion of the sequence is not shown, but is understood to begin at the end of this sequence. B_z pulses of 0.2 T are added and subtracted from the static field strength of 3.0 T.

(5.2.2) In-depth Discussion of dreMR-DIR

To appreciate how the DIR sequence works, it is useful to plot the magnetization of a group of samples during the relaxation portion of the DIR pulse sequence. In this particular example, a collection of five theoretical tissue samples was modeled. It was assumed that each sample was identical in all parameters other than the R_1'. An arbitrarily chosen R_1 value of 7 s^{-1} was used for each sample. The R_1' values were 0, -1, -2, -3 and -4 s^{-1} T^{-1}. Note that at clinical field strengths the negative magnetic field dependences in both contrast agent relaxivity (r_1) and tissue relaxation rate are typical.

The DIR sequence begins with a 90° RF saturation pulse to spoil any initial longitudinal magnetization. For the correction period, denoted P_1, the magnetization of all samples evolve together at the rate of 7 s^{-1}. At the completion of P_1 the first 180° RF pulse inverts the magnetization. Following inversion, all samples have the same magnetization. During P_2, magnetic field is increased to 3.2 T. The relaxation rates of the five samples now differ depending on the R_1 field dependence of each sample. They are 7, 6.8, 6.6, 6.4 and 6.2 s^{-1}. Each of the samples relax towards thermal equilibrium at these particular rates, with the $R_1' = 0\ s^{-1}\ T^{-1}$ sample evolving the fastest and reaching the largest magnetization upon the completion of P_2. At the completion of P_2, the second 180° RF inversion pulse inverts the magnetization. After this inversion, the $R_1' = -4\ s^{-1}\ T^{-1}$ sample has the most (least negative) magnetization. During P_3, the main magnetic field is decreased by 0.2 T so that the samples begin to relax again at the reduced magnetic field strength of 2.8 T. The relaxation rates of the samples are now: 7, 7.2, 7.4, 7.6 and 7.8 s^{-1}. For this period, the $R_1' = -4\ s^{-1}\ T^{-1}$ sample magnetizes the fastest while the $R_1' = 0\ s^{-1}\ T^{-1}$ sample magnetizes the slowest. At the instant that the $R_1' = 0\ s^{-1}\ T^{-1}$ sample crosses the zero line, the magnetization is tipped into the transverse plane with a 90° RF pulse and measured with a gradient echo sequence. The resulting magnetization is directly dependent upon R_1'.

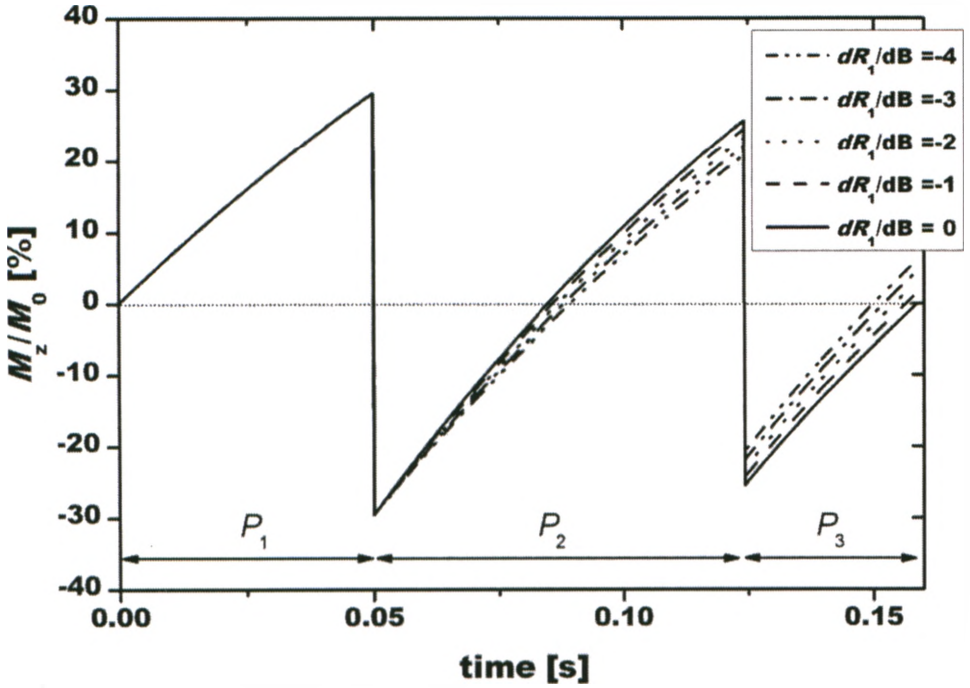

Figure 5.2. The evolution of magnetization is shown for samples with identical R_1 values (7 s^{-1}) and R_1' values varying from 0 to -4 $s^{-1} T^{-1}$. The larger the R_1' value of the sample, the greater the magnetization accrued at the end of the sequence.

The previous discussion, along with Figure 5.2, illustrated how magnetization is produced that is related to R_1'. However, it failed to explain the need for the correction period, P_1, or prove that all field independent samples will converge to zero magnetism at the end of the sequence for all *practical* values of R_1. Unless this requirement is met, no conclusions can be drawn from the sample magnetization about the binding state of the MRI contrast agent.

To address these points, the evolution of magnetization during the DIR sequence is shown again for a collection of samples having a R_1' = 0 $s^{-1} T^{-1}$, but varying in R_1 from 3 to 7 s^{-1}. Refer to Figure 5.3 during the following discussion. Because R_1 is invariant with

magnetic field strength, there is no change in the R_1 values during the pulse sequence. The magnetization of each sample evolves from zero at its particular rate during P_1. Due to differences in relaxation rates, the magnetizations begin to diverge from each other. At the completion of P_1, the first inversion pulse flips the magnetization. Following inversion, the magnetization begins to converge. The convergence occurs at some small, negative value. After converging, the magnetizations spread out again, with each sample evolving at its particular relaxation rate. At the end of P_2 the sample magnetizations are inverted once again. During P_3 the sample magnetizations begin to converge for a second time. Unlike the previous convergence, this time the magnetization lines intersect at the zero line. At the moment of intersection, image acquisition occurs and the magnetization – of which there is none – is translated into image contrast. The available magnetization is zero for all values of R_1, and all image contrast is suppressed.

Without the correction time, P_1, the second convergence of the sample magnetization lines would not occur at the zero crossing. If the final convergence fails to occur at the zero crossing then image contrast would be produced that is not due to R_1'. Remember that the point of the dreMR image is to remove any image contrast not resulting from R_1' so that any image contrast can be attributed to bound contrast agent ($\partial r_1/\partial B$).

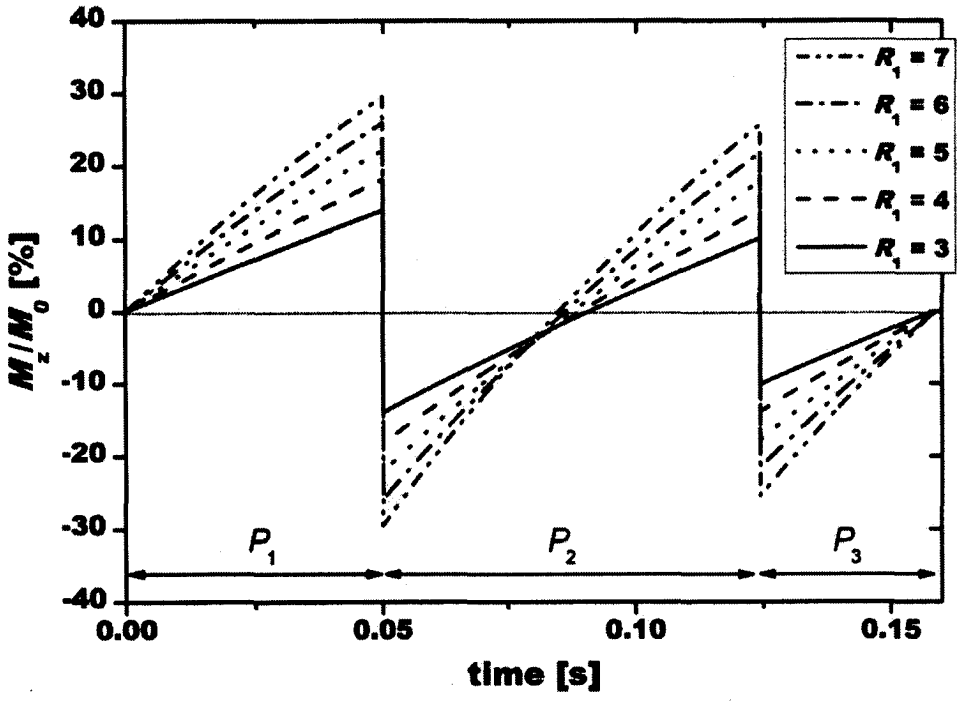

Figure 5.3. The evolution of magnetization is plotted for five samples having R_1 values from 3 to 7 s^{-1} (T_1 from 333ms to 150ms) having no magnetic field dependence ($R_1' = 0\ s^{-1}\ T^{-1}$). By appropriate choice of P_1, P_2 and P_3 the magnetization of all samples reaches zero at the end of P_3.

(5.2.3) Criteria for Determining DIR Timing Periods

For a given evolution time, $T_{ev} = P_1 + P_2 + P_3$, the optimum durations of the three DIR periods can be found by applying the following criteria to all possible combinations P_1, P_2 and P_3.

1) All samples possessing magnetic field independent relaxation rates (i.e. $R_1' \approx 0\ s^{-1}\ T^{-1}$) must have a final absolute magnetization below a specified threshold value.

Usually, the threshold value will be equal to the noise floor of the pulse sequence.

2) For a given evolution time, there may be several combinations of P_1, P_2 and P_3 that satisfy the first condition. In such cases, the combination that maximizes R_1' dependence is chosen.

(5.2.4) Optimization of Timing Periods

To accelerate the process of finding the optimum DIR timing, the magnetization at the end of the DIR sequence can be approximated by Equation 5.4. This approximation neglects the time required to ramp the magnetic field, as well as the time required to apply the 2nd inversion pulse. In Eq. 5.4 M_0 is the saturation magnetization of the sample from Curie's Law. M_1, M_2 and M_3 represent the growth of longitudinal magnetization during P_1, P_2 and P_3 respectively. The relaxation rates during the intervals P_2 and P_3 are represented by $R_{1,P2}$ and $R_{1,P3}$. Where, $R_{1,P2} = R_1 + \Delta B \frac{\partial R_1}{\partial B_0}$ and $R_{1,P3} = R_1 - \Delta B \frac{\partial R_1}{\partial B_0}$.

$$M_z(x,y,z) = \qquad [5.4]$$

$$M_0\left[(1-e^{-P_1\cdot R_1})\cdot e^{-P_2\cdot R_{1,P2}-P_3\cdot R_{1,P3}} - \frac{B0+\Delta B}{B0}(1-e^{-P_2\cdot R_{1,P2}})\cdot e^{-P_3\cdot R_{1,P3}} + \frac{B0-\Delta B}{B0}(1-e^{-P_3\cdot R_{1,P3}})\right]$$

(5.2.5) Optimization Example

To demonstrate the general relationship between the three DIR periods, the previously described optimization criteria were applied to a set of theoretical tissues having R_1 rates ranging from 1 to 10 s^{-1}. The following parameters were used in the optimization process: Static field strength (B_0) = 3.0 T, magnetic field shift (ΔB) = $\pm$ 0.2 T and a cutoff value of 1% of M_0. The 1% of M_0 cutoff value requires that the absolute magnetization of all samples must be less than 1% of M_0 at the completion of the pulse sequence. In Figure 5.4 optimum values for P_1, P_2 and P_3 are shown vs. the evolution time, T_{Ev}. The maximum allowable value of T_{Ev} for these parameters was 240 ms. Beyond 240 ms it was not possible to find any values of P_1, P_2 and P_3 that maintained all $R_1' = 0\ s^{-1}$ samples below the cutoff. To utilize sequences having T_{Ev} beyond 240 ms, either the cutoff value must be increased, or the maximum tissue relaxation rate be reduced.

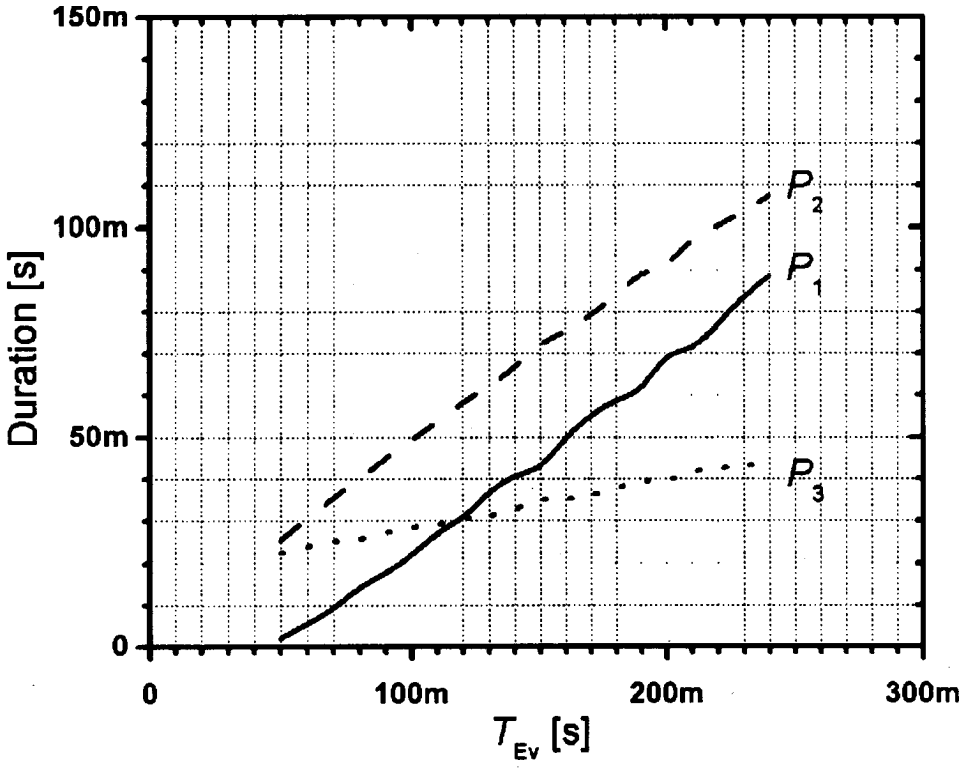

Figure 5.4. For the dreMR DIR sequence the optimum values of P_1, P_2, and P_3 are plotted versus T_{Ev}, where $T_{Ev} = P_1 + P_2 + P_3$. These optimized values are only valid at 3 T where positive and negative 0.2 T pulses have been applied during the 2nd and 3rd periods respectively.

(5.3) Methods

In the Theory section, the magnetization calculations only involved theoretical values for R_1 and R_1'. To demonstrate that the dreMR-DIR sequence can produce meaningful contrast when applied to more realistic situations, the relaxation rate curves of biological tissues (6) and the relaxivity data of a clinically available contrast agent (7,8) were incorporated into the simulation. Unlike the previous plots that displayed the evolution of magnetization, these images only indicated the *absolute* magnetization at

the completion of the sequence. Though similar in appearance to MRI images, the simulation images do not include contributions such as T_2*.

(5.3.1) Contrast Agent

For the target molecule and its corresponding targeted contrast agent, human serum albumin and MS-325 were chosen (see Figure 5.5). This choice of molecule and contrast agent was due to the availability of relaxivity data for this contrast agent rather than a particular interest in albumin. Clinically, MS-325 is used as a blood pool agent. This agent exclusively binds to albumin in order to increase the relaxivity of the agent, reducing leakage into surrounding tissues and its clearance rate from living organisms.

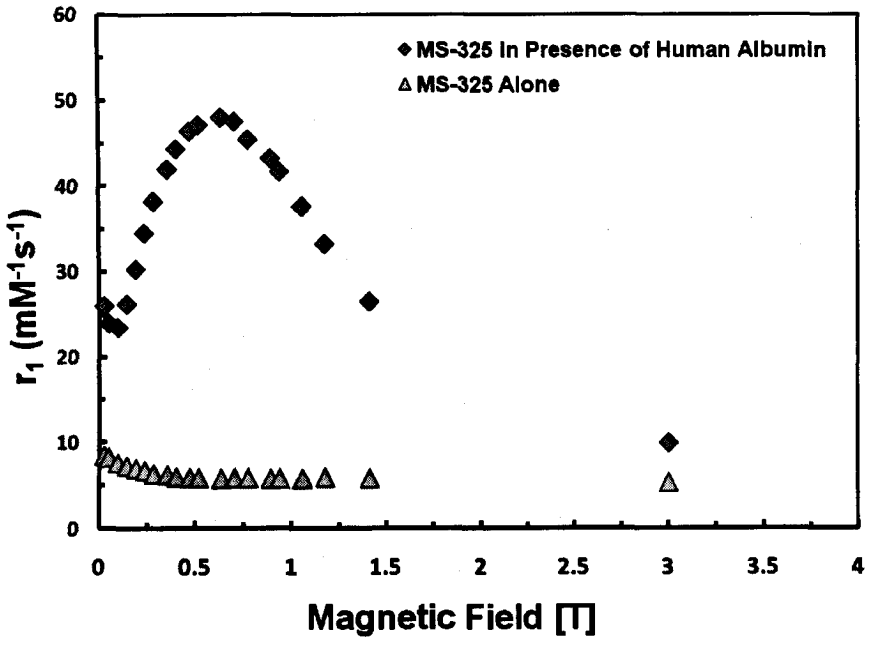

Figure 5.5. The relaxivity of a contrast agent indicates its ability to increase relaxation rates per milli mole per liter of agent. The agent MS-325 (marketed under the name Vasovist by Bayer) possess a strong field dependence only after binding to its target molecule, human serum albumin. In the unbound state the probe shows very little field dependence. Data obtained through private correspondence with Dr. Peter Caravan.

(5.3.2) Tissues

For this simulation, MS-325 relaxivity was combined with relaxation rate data for blood, adipose, muscle, white matter and grey matter (6). This datum is similar to the relaxation rates curves shown in Chapter 1 in Figure 1.5. Because only blood contains significant amounts of albumin (≈ 0.67μM), simulated binding (activation) of the agent was assumed to occur only within the blood samples. For this simulation, it was

assumed that the albumin concentration in the blood was sufficiently high enough to bind all agent molecules.

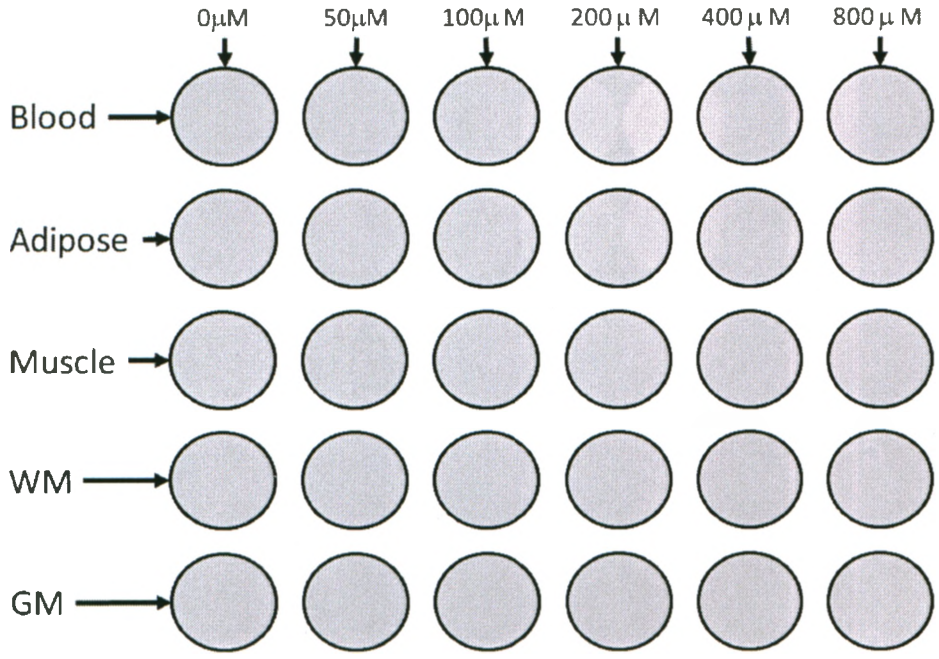

Figure 5.6. The layout of the simulated phantom is shown. From top to bottom, the rows contained: blood, adipose, muscle, white matter and grey matter. From left to right the columns contained MS-325 in the following concentrations: 0, 50, 100, 200, 400 and 800 μM.

(5.3.3) The Phantom

A simulated phantom was programmed containing blood, adipose, muscle, white matter and gray matter. See Figure 5.6. Samples were arranged in a rectangular matrix, with the tissue types changing by row and the concentration of the contrast agent increasing

by column. Across the columns, the contrast agent was added in concentrations of 0, 50, 100, 200, 400, and 800μM. The sample relaxation rates are shown in Figure 5.7.

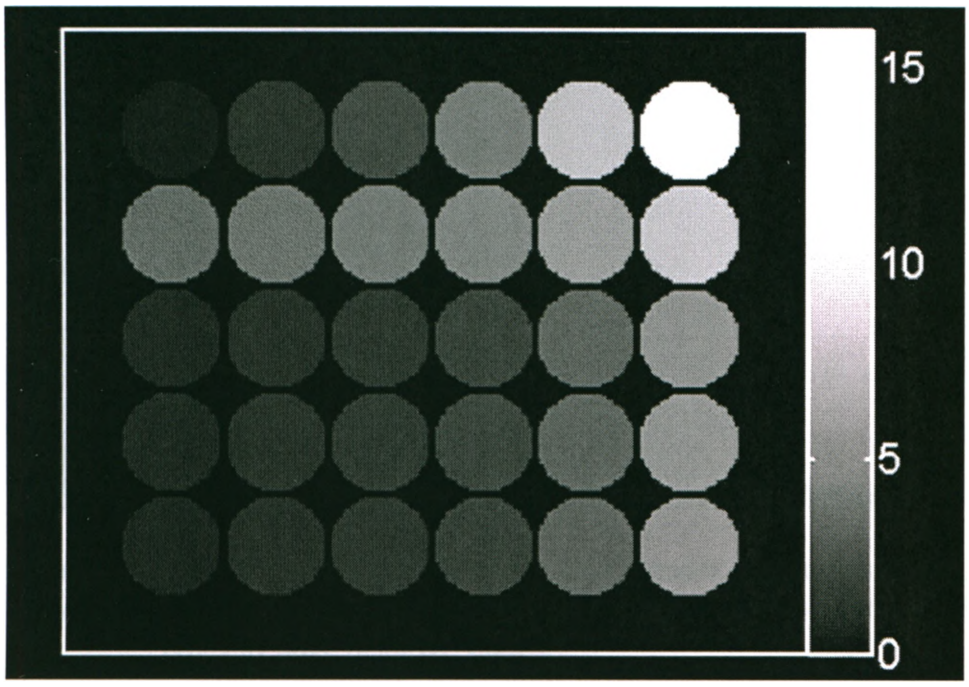

Figure 5.7. The R_1 values are shown for each sample. The adipose samples are generally bright due to their intrinsically high longitudinal relaxation rates.

The R_1' values of the samples are shown in Figure 5.8. Only the blood samples demonstrated significant change R_1' with contrast agent. In blood, the addition of 800 μM of contrast agent decreased R_1' from -0.2 to -13 $s^{-1}T^{-1}$. In non-albumin tissues, the effect was significantly less. In adipose for example, the addition of 800 μM of contrast agent only decreased R_1' from -0.4 $s^{-1}T^{-1}$ to -0.8 $s^{-1}T^{-1}$. The much greater effect in blood is due to the binding of the contrast agent to the blood's albumin.

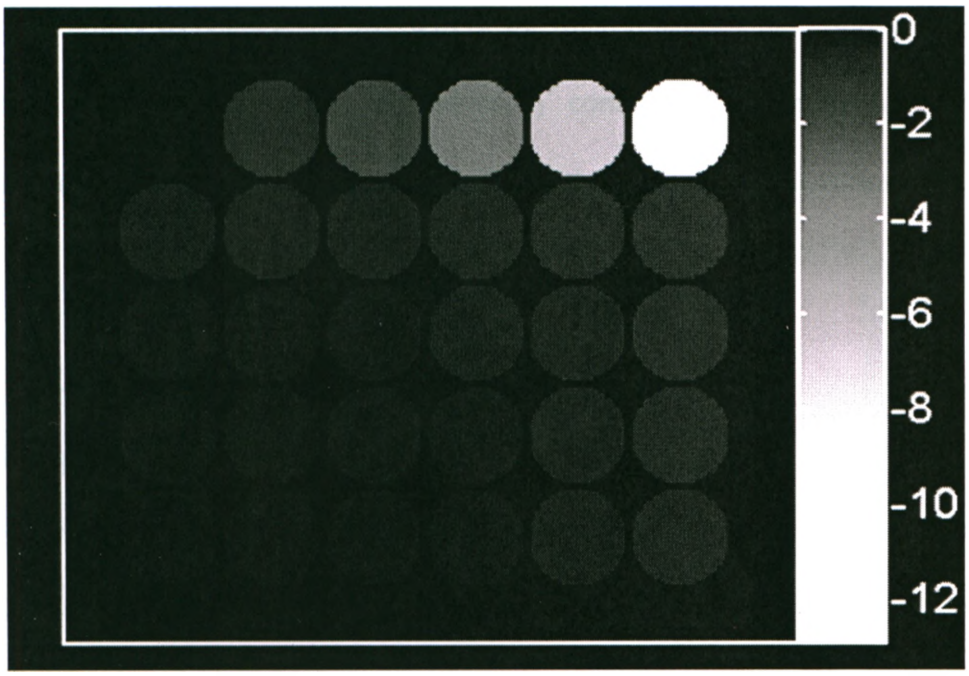

Figure 5.8. The R_1'-values are shown for each sample. Notice that R_1' is very small for all non-blood samples. At 1.5 T, relaxation rates and relaxivities typically have negative values.

(5.3.4) The dreMR-DIR Pulse Sequence

Using the criterion defined in Section 5.2.4, the dreMR periods were optimized to minimize the affect R_1 while maximizing the affect of R_1'. In this simulation, the main magnetic field strength of the MRI system was chosen to be 1.5 T, the clinical field strength where both the tissues' relaxation rate curves and contrast agent's relaxivity curves are well documented. The strength of the ΔB pulses was chosen to be 200 mT, a value easily obtainable by the dreMR insert coil discussed in Chapter 4.

(5.3.5) Removing the ΔB Pulses

Without the ability to change the strength of the main magnetic field during the image sequence, it becomes impossible to produce R_1' contrast. To demonstrate this, the previously described simulation was repeated with the bipolar ΔB pulses removed.

(5.4) Results

(5.4.1) Optimized DIR periods

For a main field strength of 1.5 T, a field shift of 0.2 T and a 1% M_0 cutoff value, the ideal dreMR-DIR timing parameters were determined to be: P_1 = 60 ms, P_2 = 77 ms and P_3 = 39 ms. The total evolution time, T_{Ev} was 172 ms. This was the longest T_{Ev}, which could be achieved with the given criterion.

(5.4.2) dreMR-DIR Image Contrast

The magnetization resulting from the double inversion recovery dreMR sequence is shown in Figure 5.9. The entire row of blood samples, with the exception of the first sample, which did not contain any contrast agent, showed significantly more magnetization than any other samples. The 2nd blood sample, with only 50 μM of contrast agent (2nd column), had a noticeably greater magnetization than the adipose sample having 16 times more contrast agent (6th column, 2nd row). The reader should note that this map illustrates the absolute magnetization. Thus, there is no

magnetization 'hiding' in the negative plane that would appear in a MRI magnitude image. Thus, magnetization has been produced that is specific to the concentration of the bound contrast agent.

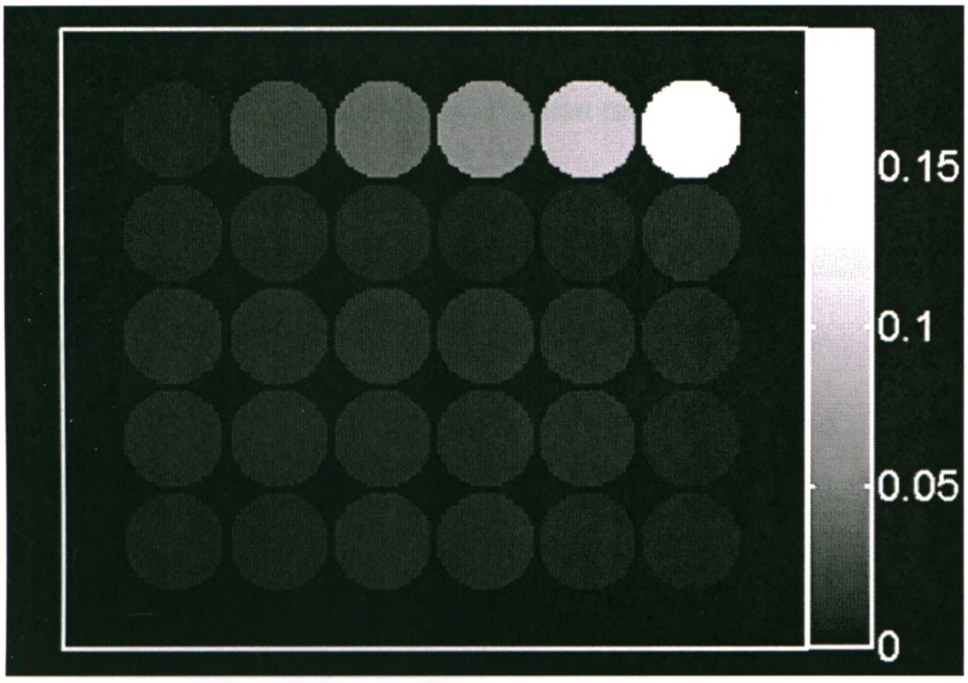

Figure 5.9. The magnetization following the end of a DIR dreMR sequence. Only the blood samples produced significant magnetization because of their large R_1' values.

(5.4.3) Non-dreMR Contrast

Figure 5.10 illustrates the effect of removing the ΔB field shifts from the DIR sequence. Unlike Figure 5.9, where image intensity was specific to the blood samples, relatively significant magnetization appeared in all tissue types. Again, the magnetization values are given in terms of M_0, with unity representing 100 % of possible magnetization.

Based upon sample intensity, it would be impossible to determine which of the samples contained albumin and which did not. The reader should not be concerned that the magnetization of some samples shown in Figure 5.10 is above the cutoff value of 1%. Removal of the ΔB field shifts changed the optimization values of the dreMR-DIR pulse sequence because it changed the pulse sequence. The important point is; without ΔB magnetic field shifts, field-dependent magnetization cannot be created.

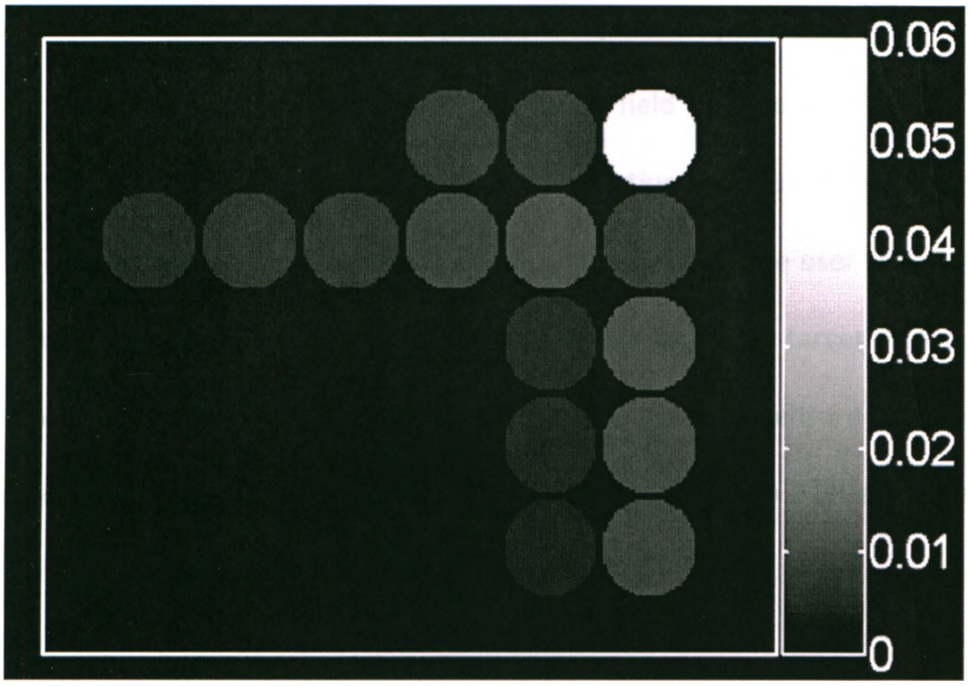

Figure 5.10. Sample magnetizations resulting from the same sequence without the ΔB pulses. Values are given in terms of M/M_0.

(5.5) Discussion

We have shown that by using the DIR sequence, magnetization may be prepared which is proportional to R_1'. Because R_1' is a strong indication of contrast agent binding, the magnetization map may be used as an indication of localized contrast agent binding. Image intensity will depend upon the concentration of the target molecule, the concentration of the contrast agent, proton density and the strength of the magnetic field shift. Comparison of Figure 5.9 and Figure 5.10 demonstrated that R_1' requires a some sort of a magnetic field shift as part of the pulse sequence. The DIR sequence cannot produce contrast related to the magnetic field dependence of the sample without a magnetic field shift during the relaxation portion of the pulse sequence.

As a molecular imaging method, dreMR DIR will enable the user to produce MR image contrast that is localized to the site of agent binding to its target molecule. Of course it will be up to the developers of the contrast agents to ensure that the agent only binds to the target. If the contrast agent incorrectly binds to a different molecule, dreMR contrast will also be produce at that site as well.

(5.6) Conclusions

It is possible to use a double inversion recovery dreMR sequence to prepare sample magnetization that is proportional to the dependence of the longitudinal relaxation rate upon magnetic field strength. Sufficient care must be taken when choosing the

relaxation periods in order to minimize the effect of R_1 on the final magnetization. By preparing magnetization that is related to R_1', MRI contrast from biological tissues and unbound contrast agents is suppressed, while contrast from tissue enhanced by bound contrast agent persists. When used with targeted contrast agents, which only demonstrate strong magnetic field dependence in the bound state, this method carries the promise of true MR-based molecular imaging.

References

1. Alford JK, Rutt BK, Scholl TJ, Handler WB, Chronik BA. Delta relaxation enhanced MR: improving activation-specificity of molecular probes through R1 dispersion imaging. Magn Reson Med 2009;61(4):796-802.
2. Caravan P, Cloutier NJ, Greenfield MT, McDermid SA, Dunham SU, Bulte JW, Amedio JC, Jr., Looby RJ, Supkowski RM, Horrocks WD, Jr., McMurry TJ, Lauffer RB. The interaction of MS-325 with human serum albumin and its effect on proton relaxation rates. Journal of the American Chemical Society 2002;124(12):3152-3162.
3. Sosnovik DE, Weissleder R. Emerging concepts in molecular MRI. Current opinion in biotechnology 2007;18(1):4-10.
4. Weissleder R, Mahmood U. Molecular imaging. Radiology 2001;219(2):316-333.
5. Overoye-Chan K, Koerner S, Looby RJ, Kolodziej AF, Zech SG, Deng Q, Chasse JM, McMurry TJ, Caravan P. EP-2104R: a fibrin-specific gadolinium-Based MRI contrast agent for detection of thrombus. Journal of the American Chemical Society 2008;130(18):6025-6039.
6. Bottomley PA, Foster TH, Argersinger RE, Pfeifer LM. A review of normal tissue hydrogen NMR relaxation times and relaxation mechanisms from 1-100 MHz: dependence on tissue type, NMR frequency, temperature, species, excision, and age. Med Phys 1984;11(4):425-448.
7. Eldredge HB, Spiller M, Chasse JM, Greenwood MT, Caravan P. Species dependence on plasma protein binding and relaxivity of the gadolinium-based MRI contrast agent MS-325. Investigative radiology 2006;41(3):229-243.
8. Rohrer M, Bauer H, Mintorovitch J, Requardt M, Weinmann HJ. Comparison of magnetic properties of MRI contrast media solutions at different magnetic field strengths. Investigative radiology 2005;40(11):715-724.
9. Goodrich KC, Hadley JR, Sung MM, Blaine AC, Timothy JS, Joshua TD, Dennis LP. Design, fabrication, and testing of an insertable double-imaging-region gradient coil. Concepts in Magnetic Resonance Part B: Magnetic Resonance Engineering 2009;35B(2):98-105.

Chapter 6 – Conclusions and Future Work

(6.1) Thesis Summary

This research demonstrated the feasibility of utilizing an insertable electromagnet to produce MRI contrast related to the magnetic field dependence of the longitudinal relaxation rate of the sample. In this work, two insert electromagnets were designed and built. The first insert was built as a prototype system and as such utilized conventional electromagnet designs and materials. Chapter 2 described the proof-of-principle experiments performed with this insert coil. A very detailed account of the design algorithms and construction processes was given in Chapter 3. The prototype coil had several shortcomings, such as significant weight, limited cooling and modest magnetic field shifts. The second generation system, described in Chapter 4, was built as a first step towards the creation of a commercial dreMR platform. This system utilized several engineering improvements including the use of hollow wire for increased cooling and a solid-state switch box to isolate the power supply from the magnet during image acquisition. These improvements resulted in an insert magnet that was smaller, lighter and capable of much larger magnetic field shifts than the prototype system. In Chapter 5, an improved dreMR pulse sequence was described. Unlike earlier dreMR sequences, dreMR-DIR sequence does not require either image subtraction or multiple images to produce dreMR images. By use of bidirectional dreMR pulses and two inversion pulses, dreMR contrast was generated directly within the pulse

sequence, removing the need for image subtraction. Though the dreMR-DIR sequence has been simulated, its actual implementation has not yet been attempted.

(6.2) Future Work

While this project has demonstrated the ability to perform true MR based molecular imaging with field-cycling technology, to be generally useful to other research groups, further hardware and software development is required. Below, several enhancements are suggested.

(6.2.1) Future Hardware Development

To be truly useful as a small animal image device, the dreMR coil requires the addition of a high-performance, small animal gradient insert set. Gradient inserts can produce gradient fields up to 1000 mT/m and achieve voxels as small as 50μm on a side (1,2). Alternatively, for human imaging, the dreMR coil would require a complete redesign to achieve an open/planar geometry. Such an insertable field-shifting magnet might resemble the planar gradient sets, which are currently under investigation by several groups (3). Finally, the internal temperature of the insert coil should be monitored at all times, and this information either interlocked with the power supply or wired to an alarm. This would prevent damage to electromagnet and MRI scanner in the event of user error or equipment malfunction.

(6.2.2) Future Software Development

In its current state, dreMR requires two computers to control the pulse sequence. All the "normal" parameters of a pulse sequence are entered into the MRI console computer, while the dreMR pulse waveform information (amplitude, duration and synchronization event) is entered into an auxiliary laptop computer. For each change in the MRI pulse sequence, which affects the timing of the pulse sequence (TR, TE, bandwidth, etc.) the dreMR waveform must be manually updated. A mistake in entering the correct information could easily result in an unusable MRI image, and even carries the possibility of damage to the dreMR insert coil.

Some efforts have already been made towards more advanced control of the dreMR waveform on Siemens' SyngoMR platform. The syngoMR platform does not possess the versatility to completely control the dreMR waveform directly, since it only has the ability to specify (control) three analog output waveforms. However, this system does have an auxiliary digital output, to permit synchronization of the MRI with other pieces of equipment. This synchronization output can be activated at any particular point within the pulse sequence, and may be used as many times as desired. To control the dreMR waveform, a two step process is used: All the waveform timing information is entered by the user directly into the MRI console. Only the amplitude waveform envelope is entered separately on a laptop computer. The MRI console

marks the start and end of the dreMR waveform with the synchronization output, automatically scaling the duration of the waveform as need.

(6.2.3) Future Applications

While platform improvements are important, dreMR's transition from an experimental device to a biomedical research tool will depend upon identifying key applications. In this section several potential uses for dreMR are discussed.

The first potential application is in the study of thrombosis. Thrombosis is the underlying pathology in numerous cardiovascular diseases with millions of people affected. These diseases, which include heart attack, ischemic stroke and pulmonary embolism, share a common cause, blood clots (thrombi). To aid in the detection of thrombi, highly specialized contrast agents such as EP-2104R (4) were developed, which will bind to fibrin contained in the clots. This coating of contrast agents causes the clots to appear brighter in MRI images. However, literature shows that the ideal delay between injection of contrast agent and imaging is two hours, the time required for the unbound contrast agent to be cleared from the body. With dreMR, it is possible to directly differentiate between image enhancements caused by the contrast agent from other sources of signal, and thus it is not necessary to wait for the unbound agent to be cleared. Reducing the time between the onset of symptoms and diagnosis could result in an immediate improvement in outcome for stroke and heart attack patients. As an added benefit, dreMR also removes the need for both pre and post contrast images.

A second potential application is the study of tumor response to chemotherapy and radiation therapies. Reactions differ with each patient, making it difficult to predict the outcome of a particular treatment. It is also widely recognized that tumor physiologies vary widely and may change with both time and treatment. DreMR may prove to be a unique tool for monitoring tumor physiology and may guide in the treatment of tumors. For example, using dreMR with the agent MS-325 may allow improved measurements of tumor permeability, which some studies suggest is an indication of tumor aggressiveness. If this hypothesis proves to be correct, then dreMR may even be able to distinguish between malignant and benign lesions.

(6.3) Conclusions

Delta relaxation enhanced MR was shown to be a viable method for performing targeted molecular imaging upon clinical, superconducting MRI platforms. Though not trivial, the design and construction of a dreMR system is well within the abilities of most research institutions. The dreMR method takes advantage of a common, though unutilized feature of targeted T_1-enhancing contrast agents, an unambiguous difference in the magnetic field dependence of longitudinal relaxivity between the bound and unbound states. We have demonstrated that by measuring the change in MR image intensity with the strength of the applied magnetic field, it is possible to determine the

location of the target molecule. As the number of targeted contrast agents increases daily, so too does the number of potential applications for dreMR.

(6.4) References

1. Foster-Gareau P, Heyn C, Alejski A, Rutt BK. Imaging single mammalian cells with a 1.5 T clinical MRI scanner. Magn Reson Med 2003;49(5):968-971.
2. Goodrich KC, Hadley JR, Sung MM, Blaine AC, Timothy JS, Joshua TD, Dennis LP. Design, fabrication, and testing of an insertable double-imaging-region gradient coil. Concepts in Magnetic Resonance Part B: Magnetic Resonance Engineering 2009;35B(2):98-105.
3. Feldman RE, Hardy CJ, Aksel B, Schenck J, Chronik BA. Experimental determination of human peripheral nerve stimulation thresholds in a 3-axis planar gradient system. Magn Reson Med 2009.
4. Overoye-Chan K, Koerner S, Looby RJ, Kolodziej AF, Zech SG, Deng Q, Chasse JM, McMurry TJ, Caravan P. EP-2104R: a fibrin-specific gadolinium-Based MRI contrast agent for detection of thrombus. Journal of the American Chemical Society 2008;130(18):6025-6039.